Check for updates

Received: 19 June 2021 | Revised: 19 October 2021 | Accepted: 19 October 2021

DOI: 10.1111/gcb.15986

Global Change Biology WILEY

TECHNICAL ADVANCE

A new open-path eddy covariance method for nitrous oxide and other trace gases that minimizes temperature corrections

Da Pan[1,2] | Ilya Gelfand[3,4,5] | Lei Tao[1,2] | Michael Abraha[3,4,6] | Kang Sun[7,8] | Xuehui Guo[1,2] | Jiquan Chen[3,6] | G. Philip Robertson[3,4,9] | Mark A. Zondlo[1,2]

[1]Department of Civil and Environmental Engineering, Princeton University, Princeton, New Jersey, USA

[2]Center for Mid-Infrared Technologies for Health and the Environmental, NSF-ERC, Princeton, New Jersey, USA

[3]Great Lakes Bioenergy Research Center, Michigan State University, East Lansing, Michigan, USA

[4]W.K. Kellogg Biological Station, Michigan State University, Hickory Corners, Michigan, USA

[5]The French Associates Institute for Agriculture and Biotechnology of Drylands, The Jacob Blaustein Institutes for Desert Research, Ben-Gurion University of the Negev, Beer-Sheva, Israel

[6]Center for Global Change and Earth Observations, Michigan State University, East Lansing, Michigan, USA

[7]Department of Civil, Structural and Environmental Engineering, University at Buffalo, Buffalo, New York, USA

[8]Research and Education in eNergy, Environment and Water (RENEW) Institute, University at Buffalo, Buffalo, New York, USA

[9]Department of Plant, Soil, and Microbial Sciences, Michigan State University, East Lansing, Michigan, USA

Correspondence
Mark A. Zondlo, CEE/Princeton Engineering Quadrangle E209A, Olden Street, Princeton, NJ 08544, USA.
Email: mzondlo@princeton.edu

Present address
Da Pan, Department of Atmospheric Science, Colorado State University, Fort Collins, Colorado, USA

Funding information
NSF, Grant/Award Number: DEB-1359538 and DEB 1832042; DOE, Grant/Award Number: DE-SC0011288 and DE-SC0018409

Abstract

Low-power, open-path gas sensors enable eddy covariance (EC) flux measurements in remote areas without line power. However, open-path flux measurements are sensitive to fluctuations in air temperature, pressure, and humidity. Laser-based, open-path sensors with the needed sensitivity for trace gases like methane (CH_4) and nitrous oxide (N_2O) are impacted by additional spectroscopic effects. Corrections for these effects, especially those related to temperature fluctuations, often exceed the flux of gases, leading to large uncertainties in the associated fluxes. For example, the density and spectroscopic corrections arising from temperature fluctuations can be one or two orders of magnitude greater than background N_2O fluxes. Consequently, measuring background fluxes with laser-based, open-path sensors is extremely challenging, particularly for N_2O and gases with similar high-precision requirements. We demonstrate a new laser-based, open-path N_2O sensor and a general approach applicable to other gases that minimizes temperature-related corrections for EC flux measurements. The method identifies absorption lines with spectroscopic effects in the opposite direction of density effects from temperature and, thus, density and spectroscopic effects nearly cancel one another. The new open-path N_2O sensor was tested at a corn (*Zea mays* L.) field in Southwestern Michigan, United States. The sensor had an optimal precision of 0.1 ppbv at 10 Hz and power consumption of 50 W. Field trials showed that temperature-related corrections were 6% of density corrections, reducing EC random errors by 20-fold compared to previously examined lines. Measured open-path N_2O EC fluxes showed excellent agreement with those made with static chambers ($m = 1.0 \pm 0.3$; $r^2 = .96$). More generally, we identified absorption lines for CO_2 and CH_4 flux measurements that can reduce the temperature-related corrections by 10–100 times compared to existing open-path sensors. The proposed method provides a new direction for future open-path sensors, facilitating the expansion of accurate EC flux measurements.

KEYWORDS
air-surface exchange flux, CH_4, CO_2, eddy covariance, laser, N_2O, open path, Trace gas sensing

This is an open access article under the terms of the Creative Commons Attribution-NonCommercial-NoDerivs License, which permits use and distribution in any medium, provided the original work is properly cited, the use is non-commercial and no modifications or adaptations are made.
© 2021 The Authors. *Global Change Biology* published by John Wiley & Sons Ltd

1 | INTRODUCTION

The eddy covariance (EC) method is the most direct approach for measuring surface–air exchange fluxes. Instrumentation advancement of nondispersive infrared (NDIR) sensors in the past few decades has greatly improved our capability for measuring carbon dioxide (CO_2), water vapor (H_2O), and energy fluxes using the EC method (Anderson et al., 1984; Auble & Meyers, 1992; Baldocchi et al., 2001; Burba et al., 2010; Goulden et al., 1996). Easy-to-use and power-efficient instruments have led to broad spatial and temporal coverages of CO_2 and H_2O flux measurements, which provide critical information for understanding and predicting carbon and energy balances of global ecosystems (Baldocchi, 2020).

Recent advances in narrowband infrared (IR) technology have enhanced our capability to measure methane (CH_4) and nitrous oxide (N_2O) fluxes—the second and third most important greenhouse gases (GHG) using the EC method (Eugster & Plüss, 2010; Huang et al., 2014; Kroon et al., 2010; McDermitt et al., 2011; Neftel et al., 2010; Zenone et al., 2016; Zona, Janssens, Aubinet, et al., 2013a; Zona, Janssens, Gioli, et al., 2013b). However, a large fraction of the CH_4 flux measurements and all of the N_2O flux observations are based on closed-path systems that require a power-hungry pump, a temperature-controlled enclosure, and labor-intensive installation and maintenance (Nemitz et al., 2018). These requirements constrain the spatial coverage of EC measurements, preventing their deployment in remote ecosystems that contribute to significant uncertainties of top-down emission estimates, such as Arctic tundra and wetlands for CH_4 and tropical and marine ecosystems for N_2O (Mastepanov et al., 2008; Montzka et al., 2011). Even in croplands, where most anthropogenic N_2O emissions occur, supplying the needed power infrastructure is challenging.

A laser-based, open-path sensor design provides high precision measurements and overcomes the power challenge but is intrinsically sensitive to ambient condition changes. McDermitt et al. (2011) developed a commercial open-path CH_4 sensor for EC measurements with a precision of five parts per billion volume (ppbv) at 10 Hz and low power consumption (<10 W), which has significantly improved spatial coverages of CH_4 flux measurements (Burba et al., 2019). However, when exposed to the ambient environment, open-path measurements are impacted by variations in atmospheric conditions, especially temperature fluctuations. Flux-induced concentration changes for long-lived GHGs could be overwhelmed by such impacts, making it almost impossible to measure small fluxes with high confidence (Burba et al., 2019; Chamberlain et al., 2017; Nemitz et al., 2018). For instance, N_2O has a high atmospheric background concentration around 330 ppbv, and flux-related fluctuations of N_2O (~0.1 ppbv without strong sources or sinks) can be one or two orders of magnitude smaller than the impacts of temperature fluctuations (a few ppbv).

Temperature effects manifest themselves in laser-based, open-path EC measurements in two ways. First, as an air parcel moves vertically, its temperature may differ from the surrounding environment, causing expansion or contraction of the air parcel (Lee & Massman, 2011). For example, when two air parcels with the same N_2O molecular density, located above and below a sensor, move toward the sensor (Figure 1a), the rising air parcel will have a lower density (expansion) than the sinking one (contraction). Trace gas density changes from the ideal gas law lead to a buoyancy flux that needs to be corrected when calculating ecosystem fluxes (Burba et al., 2019). Second, spectroscopic absorption lines themselves have a strong temperature dependence (Figure 1b). Laser-based, open-path sensors measure gas densities by detecting changes of light intensity caused by the absorption of target molecules. The laser light only interacts with molecules at certain differences of rotational-vibrational (ro-vibrational) energy levels. Therefore, the strength of the absorption line depends on the molecular population distribution of ro-vibrational energy states, which follows the Boltzmann distribution and shifts

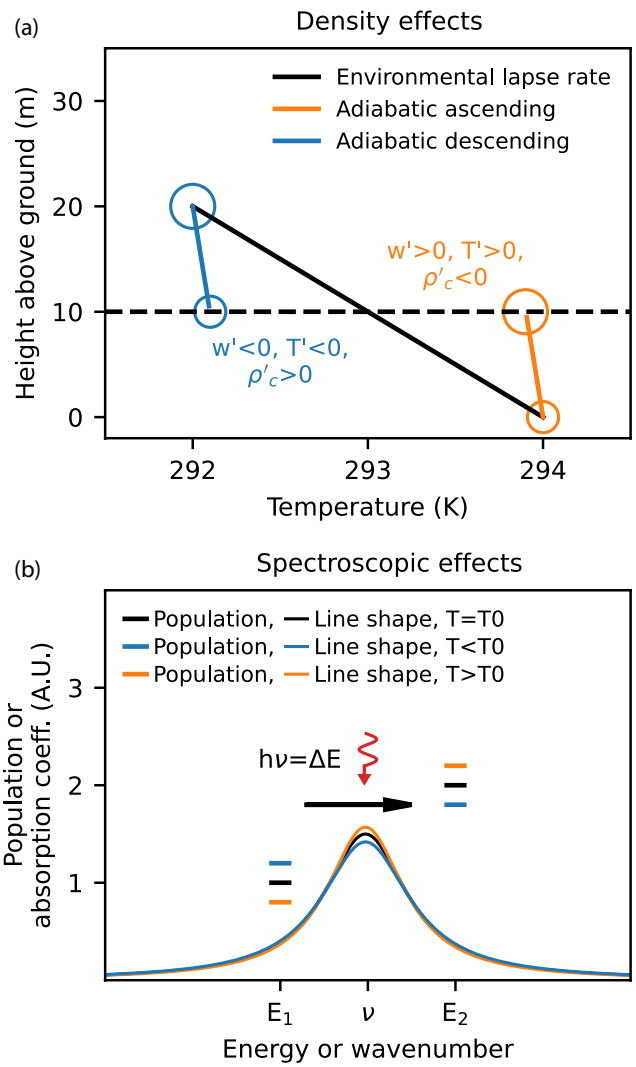


FIGURE 1 Temperature-related density effects and spectroscopic effects. Panel (a) shows expansion and contraction caused by vertical movements of air parcels, leading to density changes. Panel (b) demonstrates population shifts for different energy states and broadening effects caused by temperature variations

as temperature changes (Hanson et al., 2016). The line shape also depends on temperature because of Doppler broadening (caused by the Doppler effect of molecules with different velocities) and collision broadening (due to perturbations by collisions; Hanson et al., 2016). Therefore, measurement results from laser-based, open-path sensors are subjected to temperature-related spectroscopic effects, which also need to be accounted for estimating air–ecosystem exchange fluxes.

Corrections for temperature-related density and spectroscopic effects can lead to large random and systematic errors in fluxes. Webb et al. (1980) proposed an analytical solution to account for the density effects in post-field analysis using sensible heat flux, known as the WPL correction. Burba et al. (2019) proposed corrections for spectroscopic effects in a similar manner. The robustness of WPL and spectroscopic corrections have been examined under ideal conditions experimentally (Burba et al., 2019; Chamberlain et al., 2017; Ham & Heilman, 2003; Leuning et al., 1982). However, random and systematic errors in sensible and latent heat fluxes can propagate through corrections to corrected fluxes (Lee & Massman, 2011; Richardson et al., 2006). In addition, frequency response attenuation caused by separations and differences in the sampling paths of the instruments also needs corrections. How and when to apply the frequency response corrections during the post-processing relative to WPL and spectroscopic corrections are still under debate, and different choices could lead to significant differences in EC fluxes (Burba et al., 2019; Chamberlain et al., 2017; Lee & Massman, 2011; Nakai et al., 2020).

Because of the large random and systematic errors due to temperature corrections, open-path EC measurements of gases with small fluxes are considered uncertain and of limited use (Nemitz et al., 2018). Particularly, trace gases that have pulse emissions followed by extended low-flux periods, such as N_2O, could lead to large biases for long-term measurements (Chamberlain et al., 2017). Burba et al. (2019) estimated that temperature-related density and spectroscopic corrections could be 50 and −30 to 80 times the background N_2O flux, respectively.

One way to mitigate these temperature effects is to choose spectroscopic lines such that the temperature-related spectroscopic and density corrections have different signs but similar magnitudes, and therefore, the net temperature correction is minimized. Exploring this possibility, we demonstrate a new quantum cascade laser (QCL)-based, open-path N_2O sensor, which was tested in a maize field at the Kellogg Biological Station (KBS), Michigan, United States. The method also minimizes systematic errors arising from separate locations of the temperature and trace gas measurements as the underlying physical processes related to temperature changes occur simultaneously in the same sensing volume. The sensing approach allows for accurate measurements of N_2O fluxes, despite the inherent small fluctuation on a large background. The temperature minimization approach is applicable to other trace gas fluxes, and nominal absorption lines for CO_2 and CH_4 measurements are also identified.

2 | MATERIALS AND METHODS

2.1 | Correction terms for laser-based open-path instrument

The EC method calculates flux as the covariance of turbulent parts of vertical wind and gas concentration ($\overline{w'\rho_c'}$). Temperature-related corrections as well as corrections for pressure- and H_2O-related effects can be expressed following Burba et al. (2019):

$$\begin{aligned} F_c = {} & \bar{k}\left(\overline{w'\rho_{cm}'} + \mu\frac{\overline{\rho_{cm}}}{\overline{\rho_d}}\overline{w'\rho_v'} + \left(1+\mu\frac{\overline{\rho_v}}{\overline{\rho_d}}\right)\frac{\overline{\rho_{cm}}}{\overline{T}}\overline{w'T'} - \left(1+\mu\frac{\overline{\rho_v}}{\overline{\rho_d}}\right)\frac{\overline{\rho_{cm}}}{\overline{p}}\overline{w'p'}\right) \\ & + \overline{w'k'}\overline{\rho_{cm}} = \overline{w'\rho_{cm}'} + \mu\frac{\overline{\rho_c}}{\overline{\rho_d}}\overline{w'\rho_v'} + \left(1+\mu\frac{\overline{\rho_v}}{\overline{\rho_d}}\right)\frac{\overline{\rho_c}}{\overline{T}}\overline{w'T'} - \left(1+\mu\frac{\overline{\rho_v}}{\overline{\rho_d}}\right)\frac{\overline{\rho_c}}{\overline{p}}\overline{w'p'} \\ & + \left(\overline{w'k'}\overline{\rho_{cm}} + (\bar{k}-1)\overline{w'\rho_{cm}'}\right) = \overline{w'\rho_{cm}'} + F_{d,v} + F_{d,T} + F_{d,p} + F_s, \end{aligned} \tag{1}$$

where F_c is the corrected flux (μg·m^{-2}·s^{-1}); w is the vertical wind (m·s^{-1}); ρ_{cm} is the measured gas density (μg·m^{-3}); μ is the ratio of molar masses of air to water; ρ_d is dry air density (μg·m^{-3}); ρ_v is H_2O density (μg·m^{-3}); T is the air temperature (K); and p is the pressure (Pa). k is a predetermined spectroscopic correction coefficient that relates measured gas density to actual gas density as $\rho_c = k\left(T, p, \rho_v\right)\rho_{cm}$. $F_{d,v}$, $F_{d,T}$, and $F_{d,p}$ are H_2O-, temperature-, pressure-related density corrections, respectively, taking account of the mean spectroscopic effect ($\bar{k}$). F_s is the spectroscopic correction. More details and derivation of Equation (1) can be found in Lee and Massman (2011) and Burba et al. (2019). Table 1 summarizes the causes and impacts of these corrections.

Ignoring nonlinear dependency of k on T, p, and ρ_v and corresponding higher order terms (i.e., $\overline{w'T'T'}$), Equation (1) can be rearranged as:

$$\begin{aligned} F_c = {} & \bar{k}\left(\overline{w'\rho_{cm}'} + F_{d,v} + F_{d,T} + F_{d,p}\right) + k_T\overline{\rho_{cm}}\overline{w'T'} + k_v\overline{\rho_{cm}}\overline{w'\rho_v'} + k_p\overline{\rho_{cm}}\overline{w'p'} \\ = {} & \bar{k}\overline{w'\rho_{cm}'} + M_vF_{d,v} + M_TF_{d,T} + M_pF_{d,p}, \end{aligned} \tag{2}$$

with

$$\begin{aligned} M_v &= \bar{k} + \frac{\overline{\rho_d}}{\mu}k_v \\ M_T &= \bar{k} + \frac{\overline{T}}{1+\mu\frac{\overline{\rho_v}}{\overline{\rho_d}}}k_T \\ M_p &= \bar{k} - \frac{\overline{p}}{1+\mu\frac{\overline{\rho_v}}{\overline{\rho_d}}}k_p \end{aligned}, \tag{3}$$

where $k_v = \partial k/\partial\rho_v|_{v=\bar{v}}$, $k_T = \partial k/\partial T|_{T=\bar{T}}$, and $k_p = \partial k/\partial p|_{p=\bar{p}}$. M_v, M_T, and M_p are the H_2O concentration, temperature, and pressure multipliers that adjust the corresponding density corrections (i.e., $F_{d,v}$, $F_{d,T}$, and $F_{d,p}$) to incorporate spectroscopic effects. Equation (2) is a first-order approximation of Equation (1) and effectively estimates the magnitudes of net corrections (sum of spectroscopic and density corrections) in terms of density corrections and the raw covariances (i.e., $\overline{w'T'}$, $\overline{w'p'}$, and $\overline{w'\rho_v'}$). For example, $M_T = 1$ means

TABLE 1 Causes, expressions, and impacts of density and spectroscopic effects on measurements from laser-based, open-path N_2O sensors and corresponding flux corrections

	Density effects			Spectroscopic effects			Net effects		
	Concentration changes (background fluctuations <0.03%)								
Formular	$\rho_c = \frac{\chi_c(p-e)}{R_c T}$			$\rho_{cm} = \rho_c / k$			$\rho_{cm} = \frac{\chi_c(p-e)}{R_c T k}$		
Cause	***T* increase (1°C)**	***e* increase (1 hPa)**	***p* increase (1 hPa)**	***T* increase (1°C)**	***e* increase (1 hPa)**	***p* increase (1 hPa)**	***T* increase (1°C)**	***e* increase (1 hPa)**	***p* increase (1 hPa)**
Impact (%)	−0.33%	−0.1%	0.1%	−0.33% to 1%[a]	−0.06%[b]	−0.13%[c]	−0.66% to 0.66%[a]	−0.16%	−0.03%
	Flux corrections (background flux ~0.02 mg N_2O-N m^{-2} h^{-1})								
Formular	$\overline{k}\left(F_{d,T} + F_{d,v} + F_{d,p}\right)$			$F_s = \overline{w'k'}\overline{\rho_{cm}} + (\overline{k}-1)\overline{w'\rho'_{cm}}$[d]			$\overline{k}\left(F_{d,T} + F_{d,v} + F_{d,p}\right) + F_s$		
Cause	Thermal expansion/ contraction	H_2O dilution	*p*-related expansion/ contraction	*T*-related line strength and line profile changes	H_2O broadening	Air broadening	Net *T*-related effects	Net H_2O-related effects	Net *p*-related effects
Formular for each term	$\left(1+\mu\frac{\overline{\rho_v}}{\overline{\rho_d}}\right)\frac{\overline{\rho_c}}{\overline{T}}\overline{w'T'}$	$\mu\frac{\overline{\rho_c}}{\overline{\rho_d}}\overline{w'\rho'_v}$	$-\left(1+\mu\frac{\overline{\rho_v}}{\overline{\rho_d}}\right)\frac{\overline{\rho_c}}{\overline{p}}\overline{w'p'}$	$k_T\overline{\rho_{cm}}\overline{w'T'}$	$k_v\overline{\rho_{cm}}\overline{w'\rho'_{cm}}$	$k_p\overline{\rho_{cm}}\overline{w'p'}$	$M_T F_{d,T}$	$M_v F_{d,v}$	$M_{d,p} F_{d,p}$
Impact	5500%	900%	400%	−5500% to 16500%[a]	600%[b]	−500%[c]	−11000% to 11000%[a]	1400%[b]	−100%[c]

Note: The impacts are estimated based on results from Burba et al. (2019) and Lee and Massman (2011) at 25°C and 1013 hPa for background flux of 0.02 mg N_2O-N m^{-2} h^{-1}. ρ_c, ρ_d, and ρ_v are mass densities of the target gas, dry air, and water vapor, respectively. ρ_{cm} is the mass density of the target gas measured by laser-based, open-path sensor. χ_c is the mixing ratio of the target gas. *T*, *e*, and *p* are ambient temperature, water vapor pressure, and pressure. R_c is the gas constant for the target gas. *k* is the spectroscopic coefficient. *w* is the vertical wind component. $F_{d,T}$, $F_{d,v}$, and $F_{d,p}$ are the temperature-, H_2O-, and pressure-related density corrections. F_s is the spectroscopic correction. μ is the molar mass ratio of dry air and water vapor. $k_T = \partial k/\partial T|_{T=\overline{T}}$, $k_v = \partial k/\partial \rho_v|_{v=\overline{v}}$, and $k_p = \partial k/\partial p|_{p=\overline{p}}$ are the linear sensitivities of *k* to temperature, water vapor concentration, and pressure changes at given *T*, ρ_v, and *p*. M_T, M_v, and M_p are temperature, H_2O concentration, and pressure multipliers that adjust the corresponding density corrections (i.e., $F_{d,v}$, $F_{d,T}$, and $F_{d,p}$) to incorporate spectroscopic effects.

[a]Estimated for N_2O lines from 4.4 to 4.6 μm.

[b]Estimated using measured H_2O-broadening coefficient of the 4.542 μm N_2O line.

[c]Estimated using air-broadening coefficient of the 4.542 nm N_2O line.

[d]Mean spectroscopic correction effect on the measured flux term ($(\overline{k}-1)\overline{w'\rho'_{cm}}$) is usually small (<5%) and is ignored for estimating temperature-, H_2O-, and pressure-related corrections.

[e]Although net H_2O-related effect and correction are large compared to N_2O background flux, the associated errors can be reduced by simultaneously measuring H_2O (e.g., using 4.546 μm N_2O line).

that temperature corrections are due to $F_{d,T}$ only with no spectroscopic effects, which is the case for NDIR CO_2 and H_2O sensors (Burba et al., 2019). M_T decreases when temperature-related spectroscopic effects impact ρ_{cm} in the opposite direction of density effects, and $M_T = 0$ indicates no temperature effects. Therefore, minimizing $|M_T|$ is equivalent to reducing the net temperature-related correction.

Using Equation (2) may lead to errors when $k\left(T, p, \rho_v\right)$ has a significant nonlinear dependence on T, p, and ρ_v. However, higher order covariance terms, such as $\overline{w'T'T'}$, often are much smaller than flux terms and can be ignored. Therefore, the nonlinear dependency of k has a limited impact on M_T and temperature-related corrections. Nevertheless, using Equation (1) can reduce associated errors leading to more accurate results.

2.2 | Line selection and sensor development method

Figure 2 outlines the conventional and the proposed method for absorption line selection and sensor development using N_2O as an example. Figure 2a shows the strongest absorption lines of N_2O in its fundamental band. Conventionally, line strength, interferences from other gases, and availability of laser wavelengths are the major factors influencing line selection for a laser-based sensor (Figure 2d). We propose two additional steps for optimizing open-path, laser-based sensors. First, as shown in Figure 2b, M_T is estimated for these N_2O lines using spectroscopic simulations at a reference temperature (25°C). More details about the simulations and associated uncertainties are provided in SI Section I. An ideal

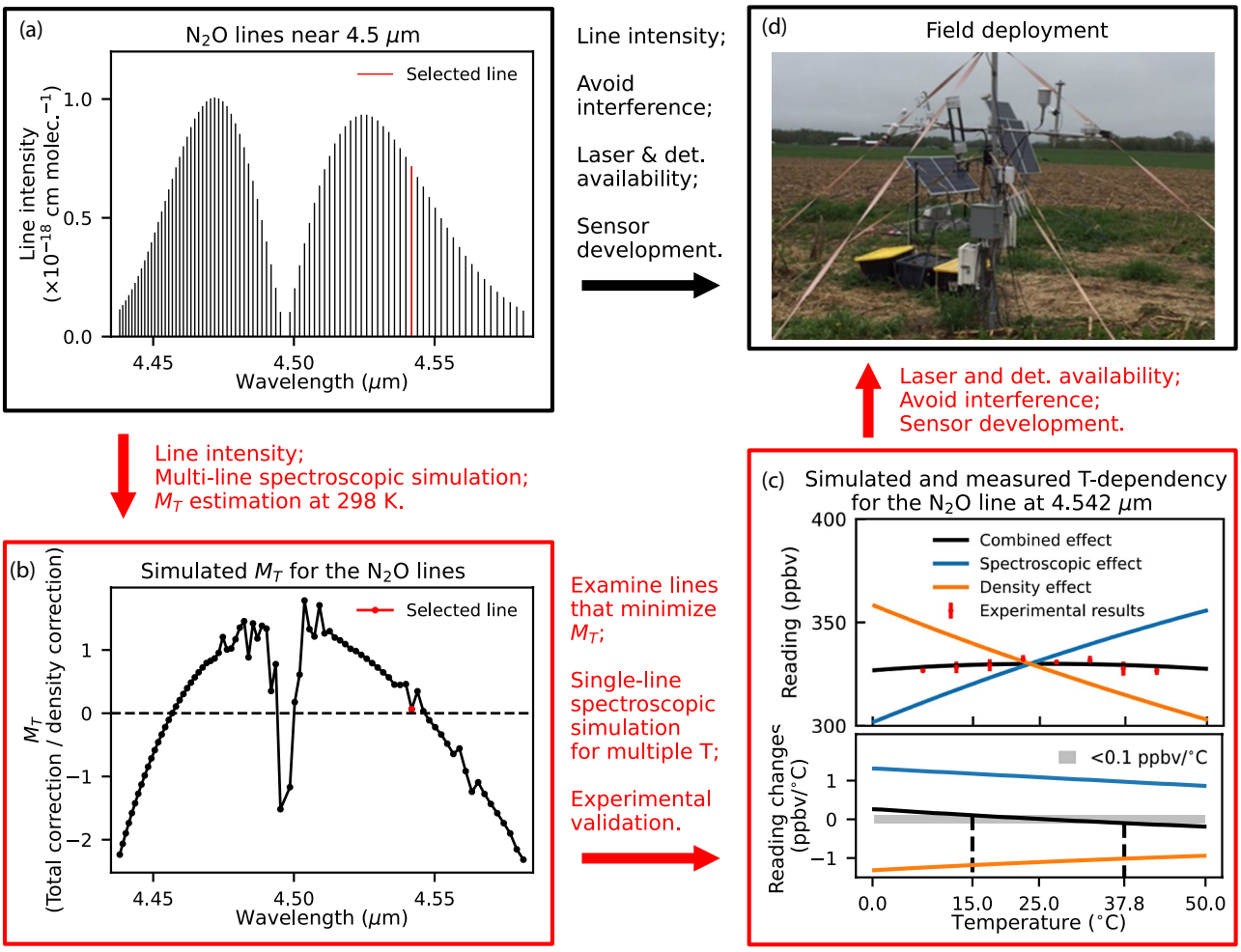


FIGURE 2 The conventional and proposed methods for sensor development. The conventional method, which considers absorption line intensity, interference from other gases, and laser and detector availability, is shown by black boxes (panels (a) and (d)) and the black arrow. Red boxes (panels (b) and (c)) and red arrows show the added steps of the proposed method. Panel (b) shows the simulated temperature multipliers (M_T) at 25°C, and the red line shows the selected absorption line that minimizes $|M_T|$. Panel (c) shows detailed simulations at different temperatures and laboratory validation of the simulations for the selected line (4.542 μm). The simulations and laboratory tests are for the wavelength modulation spectroscopy peak-to-trough height method. Using different methods may lead to different results and line selections

line as described previously has M_T close to zero, and the lines at 4.458, 4.542, and 4.546 μm have $|M_T|$ of <0.1 at 25°C (Table 2). We used the 4.542 μm line to develop the open-path N_2O sensor. H_2O-induced broadening effects of the 4.542 μm line were investigated experimentally (SI Section II). To confirm the line is insensitive to temperature variations, detailed simulations were conducted at a range of temperatures. The simulated readings for 330 ppbv N_2O appear less sensitive to temperature than those impacted by density and spectroscopic effects individually (Figure 2c). From 15 to 38°C, the simulated changes caused by 1°C temperature change are smaller than the optimal 10 Hz precision of the open-path N_2O sensor (0.10 ppbv). The simulation results were verified through a laboratory experiment (Figure 2c; SI Section III).

Note that M_T is a function of T, and $|M_T|$ changes when the temperature changes. Therefore, $|M_T|$ may no longer be minimized for a temperature different from the reference. M_T was also simulated for the lines at 0 and 50°C (Table 2), and the changes in M_T are usually small (±0.2) for typical seasonal temperature variations (±25°C). Nonetheless, if needed, absorption lines that minimize $|M_T|$ at extreme temperatures would likely be an adjacent absorption line that could be readily tuned with the same laser.

2.3 | Open-path N_2O sensor and field tests

As a proof of concept, a QCL-based, open-path N_2O sensor was developed to measure EC flux using the optimal 4.542 μm N_2O line. The

TABLE 2 CO_2, CH_4, and N_2O lines that are insensitive to temperature fluctuations when the wavelength modulation spectroscopy peak-to-trough height method is used

Species	Conc. ppmv	Flux mg m^{-2} h^{-1}	$F_{d,T}$ mg m^{-2} h^{-1}	Line		M_T	Net temperature-related correction	
				Wavenumber cm^{-1}	Wavelength nm		mg m^{-2} h^{-1}	% of final flux
CO_2	391	720	1434	3590.78	2784.91	0.11 (−0.10, 0.33)	161	22
				3631.84	2753.43	0.02 (−0.18, 0.23)	26	4
				6205.34	1611.52	0.03 (−0.20, 0.21)	46	6
				6246.30	1600.95	0.01 (−0.19, 0.23)	7	1
				6226.34[d]	1606.08[d]	1.49[d]	2137[d]	297[d]
CH_4	1.81	3.00	2.46	2948.11	3392.01	0.08 (−0.10, 0.25)	0.20	7
				3104.57	3221.05	−0.08 (−0.19, 0.11)	−0.20	−7
				5915.00	1690.62	−0.13 (−0.34, 0.07)	−0.31	−10
				6096.42	1640.31	−0.13 (−0.34, 0.07)	−0.33	−11
				6057.08[d]	1650.96[d]	1.44[d]	3.54[d]	118[d]
N_2O	0.31	0.020	1.130	2199.74	4546.00	0.033 (−0.204, 0.248)	0.037	187
				2201.75	4541.84	0.065 (−0.122, 0.265)	0.074	369
				2243.76	4456.80	0.002 (−0.231, 0.213)	0.003	14
				2229.43[d]	4485.45[d]	1.54[d]	1.74[d]	8701[d]
	%	g m^{-2} h^{-1}	g m^{-2} h^{-1}	cm^{-1}	nm		g m^{-2} h^{-1}	% of final flux
H_2O[e]	1.5	290.0	22.0	2200.31	4544.82	−3.41 (−3.94, −2.97)	−75.0	−26
				3590.24	2785.33	−1.40 (−0.45, −5.53)	−30.8	−11
				3632.28	2753.09	−1.10 (−1.58, −0.72)	−24.2	−8
				2936.97	3404.87	−1.65 (−1.98, −1.35)	−36.2	−12
				3103.02	3222.67	0.95 (0.88, 1.02)	20.9	7
				5915.15	1690.57	−3.42 (−3.85, −2.92)	−75.3	−26
				6244.72	1601.35	0.08 (−0.27, 0.09)	1.7	1

Note: Magnitudes of fluxes and temperature-related correction (for H = 200 W/m^2, ambient pressure of 101 kPa, and 25°C) for CO_2, CH_4, and N_2O are the same as listed in Burba et al. (2019) table 5 for intercomparison. $F_{d,T}$ is temperature-related density correction, and M_T is the temperature multiplier that adjusts temperature-related density correction to incorporate temperature-related spectroscopic correction. M_T listed in the table and the two values in the brackets are estimated for 25, 0, and 50°C, respectively.

[a]Absorption lines and results adapted from Burba et al. (2019) for the comparison at 25°C.

[b]H_2O lines near CO_2, N_2O, and CH_4 lines.

measurement principle of the N_2O sensor has been described by Tao et al. (2012) and is briefed here. Wavelength modulation spectroscopy was implemented to enhance the signal-to-noise ratio and reduce interferences from other lines. A Herriot multi-pass cell achieved a total path length of 18.9 m with a cell base length of 0.3 m. The total uncertainty of the N_2O measurements was estimated at 0.15 ppbv ± 10%. The ambient N_2O line itself was used to lock the laser scanning range from drifting. The sensor was calibrated, and the stability of the sensor was examined using N_2O standard gases before and after the field trials in an environmental chamber (SI Section IV).

The open-path N_2O sensor was installed on an EC tower along with an LI-7500 CO_2/H_2O analyzer (LI-COR Biosciences Inc.) and a CSAT3 3D sonic anemometer (Campbell Scientific Inc.) at the US-KM1 site of the Great Lakes Bioenergy Research Center's Scale-up Experiment at the Kellogg Biological Station in the summers of 2015 and 2016. Figure 2d shows the setup of the tower, and the instrument height was maintained at 1.5–2.0 m above the average canopy height. The field was converted to no-till continuous maize in 2009 from a USDA Conservation Reservation Program grassland, where the dominant vegetation was smooth bromegrass (Abraha et al., 2018). Urea ammonium nitrate (28% liquid N: ~180 kg N ha^{-1} $year^{-1}$) fertilizers were applied by a split application during planting in May and by side dressing in mid-June (Abraha et al., 2018).

EC fluxes were calculated at 30-min intervals following the framework proposed by Mauder et al. (2013). Modifications were made to investigate spectroscopic and density corrections. N_2O fluxes were calculated using both Equations (1) and (2). Temperature measurements from the CSAT3 were used for temperature-related corrections, and H_2O measurements from the LI-7500 were used for H_2O-related corrections. Pressure-related corrections were neglected in this study because of lacking high-frequency pressure measurements as in most EC flux studies (Burba et al., 2019). Using an NDIR CO_2 sensor, Zhang et al. (2011) showed that the pressure-related density correction accounted for 20% of the annual net ecosystem production of a forest in China. However, the pressure-broadening effect for the laser-based system could offset the impact of the pressure-related density effect, as shown in Table 1, leading to smaller errors.

Conventionally, random errors of corrected fluxes are calculated by applying the relative errors of raw covariances to fully corrected fluxes (Mauder et al., 2013), which could create significant biases in random errors when corrections overwhelm the true fluxes. For a sensor subjected to strong thermal density effects, the signal-to-noise ratio would be higher than a sensor insensitive to such effects, even if they have the same intrinsic measurement precision. Consequently, lower random errors would be assigned to the more temperature-sensitive measurements than those from a sensor insensitive to temperature variations. This is because the errors caused by corrections are ignored in this case. To account for this, we considered random errors propagated through corrections:

$$\sigma_{F_c} = \sqrt{\overline{k}^2\sigma^2_{\overline{w'\rho'_{cm}}} + M_v^2\sigma^2_{F_{d,v}} + M_T^2\sigma^2_{F_{d,T}}} = \sqrt{\overline{k}^2\sigma^2_{\overline{w'\rho'_{cm}}} + M_v^2\left(\mu\frac{\overline{\rho_{cm}}}{\overline{\rho_d}}\right)^2\sigma^2_{\overline{w'\rho'_v}} + M_T^2\left(1+\mu\frac{\overline{\rho_v}}{\overline{\rho_d}}\right)\frac{\overline{\rho_{cm}}}{\overline{T}}\sigma^2_{\overline{w'T'}}}, \quad (4)$$

where $\sigma_{\overline{w'\rho'_{cm}}}$, $\sigma_{\overline{w'\rho'_v}}$, and $\sigma_{\overline{w'T'}}$ are the random errors of high-frequency attenuation corrected covariances of corresponding terms. Caveats of using Equation (4) are discussed in Section 3; details about EC calculations and quality controls are provided in SI Section V.

Soil N_2O fluxes were also measured using the static chamber (SC) method (Holland et al., 1999; Oates et al., 2016). All SC measurements took place after 10:00 and before 16:00 local time. SC fluxes measured at multiple locations were averaged spatially to compare with N_2O EC fluxes. Because there were temporal gaps in the EC measurements due to instrument issues and non-ideal atmospheric conditions for the EC method, mean N_2O EC fluxes within a time window of ±2 h of the corresponding SC measurement were used for the comparisons. Details about SC measurements and uncertainty estimation are provided in SI Sections VI.

3 | RESULTS AND DISCUSSIONS

3.1 | Measured N_2O fluxes

In-field precision (Allan deviation) of the open-path N_2O sensor was estimated to be 0.10 ppbv at 10 Hz in 2015 and 0.15 ppbv at 10 Hz in 2016 at the beginnings of the field deployments (Figure S11),

TABLE 3 Diel means (daytime (07:00–19:00) means) of N_2O fluxes and corrections measured during 2015 and 2016 deployments

Year	Raw N_2O flux ($\overline{w'\rho'_{cm}}$)	Corrected N_2O flux (F_c)	Detection limit ($1.96\sigma_{F_c}$, 95% CI)	Spectroscopic correction (F_s)	Density correction[a] ($F_{d,T} + F_{d,v}$)	Net correction[b] ($F_s + F_{d,T} + F_{d,v}$)	Temperature-related correction ($M_T \cdot F_{d,T}$)	H_2O-related correction ($M_v \cdot F_{d,v}$)
2015	0.45 (0.75)	0.52 (0.84)	0.14 (0.20)	−0.16 (−0.33)	0.23 (0.42)	0.07 (0.10)	0.01 (0.02)	0.05 (0.08)
2016	0.07 (0.11)	0.14 (0.20)	0.06 (0.08)	−0.17 (−0.35)	0.24 (0.45)	0.07 (0.10)	0.02 (0.03)	0.06 (0.08)

Note: The unit of the fluxes and corrections is mg N_2O-N·m^{-2}·h^{-1}. $F_{d,T}$ and $F_{d,v}$ are temperature- and H_2O-related density corrections, respectively. Pressure-related density correction is ignored here. F_s is spectroscopic correction. M_T and M_v are the temperature and H_2O multipliers that adjust density corrections to incorporate spectroscopic corrections.

[a]Pressure-related density correction is ignored in this study.

[b]The net correction was calculated using Equation (1), which may be different from the sum of $M_T \cdot F_{d,T}$ and $M_v \cdot F_{d,v}$ because of the nonlinear dependency of k to H_2O concentration and temperature.

comparable to state-of-the-art closed-path sensors used in previous N_2O EC flux studies of Nemitz et al. (2018). Figure S6 shows the time series of N_2O concentrations and N_2O fluxes measured by EC and SC methods. Although the in-field power consumption was 30–50 W, power management issues related to solar panels led to large data gaps. N_2O emissions after planting and fertilization were captured in 2015 but not in 2016. Consequently, the diel mean N_2O EC flux in 2015 was four times those in 2016 (Table 3), highlighting the importance of capturing episodic N_2O emissions. Clear diel changes with high fluxes in the daytime, especially in the afternoon, were observed in 2015 and 2016 (Figure 3). Such a diel change has also been reported by Huang et al. (2014) and Zona et al. (2013b) for agricultural lands. The diel means of flux detection limit (95% CI) were 140 and 60 μg N_2O-N m^{-2} h^{-1} in 2015 and 2016, respectively. The diel means of flux detection limit due to instrument errors were smaller (30–50 μg N_2O-N m^{-2} h^{-1}) and comparable to previous studies (Kroon et al., 2007; Neftel et al., 2010; and Huang et al., 2014). These instrument error-related detection limits also fall in the mid-range of expected N_2O fluxes (1.2–120 μg N_2O-N m^{-2} h^{-1}) estimated by Nemitz et al. (2018). Details about measured EC fluxes, flux detection limits, and cospectra analyses of EC measurements are provided in SI Section VII, VIII, and IX, respectively.

Fluxes measured by SC and EC methods showed a good agreement with an R^2 of .96, a slope of 1.0 ± 0.3 (95% CI), and a bias of 22 ± 43 μg·m^{-3} (Figure 4). EC fluxes were slightly higher than the SC fluxes, especially for low flux periods in 2016. Previous N_2O EC measurements conducted with a closed-path system reported that SC observations were 20% lower than EC observations (Wang et al., 2013). Changing the temporal pairing window from ±2 to ±1 h and ±3 h leads to regression slopes of 1.2 ± 0.4 and 1.1 ± 0.3, respectively (SI Section X). Therefore, it is unclear whether the differences were caused by biases of SC flux measurements (e.g., neglecting pressure-related corrections), biases of spectroscopic and density corrections for the EC fluxes, or temporal mismatch between the two methods.

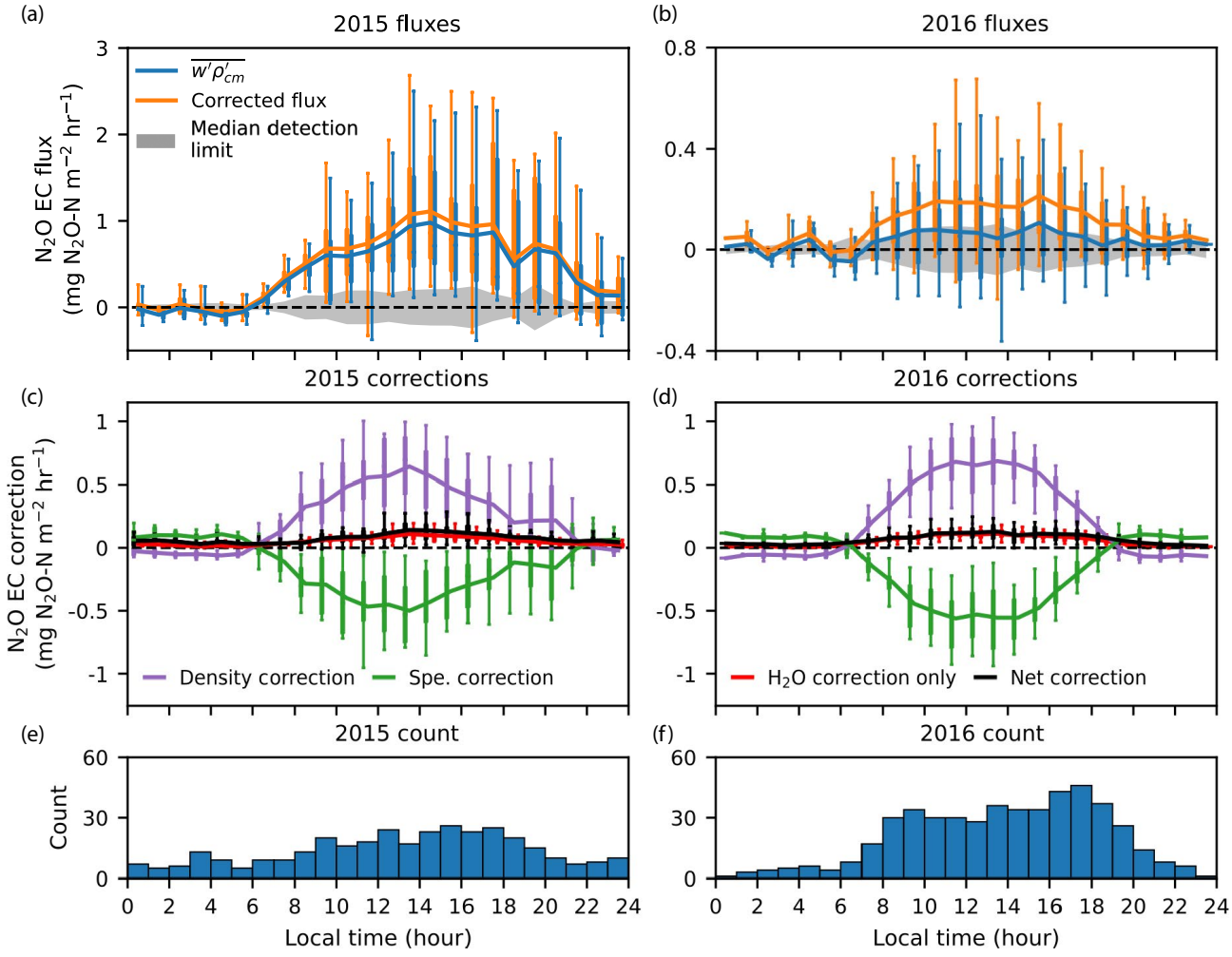


FIGURE 3 Diel variations of N_2O fluxes, flux corrections, and counts of valid observations. Panels (a) and (b) show the diel patterns of raw and corrected N_2O fluxes observed in 2015 and 2016. The bars and whiskers show 5th, 25th, 50th, 75th, and 95th percentiles of hourly composite data. The grey areas show the median detection limits ($1.96\sigma F_c$, 95% CI). Corrected EC fluxes were calculated using Equation (1). Panels (c) and (d) show density corrections ($F_{d,T} + F_{d,v}$ in Equation 1, purple) and spectroscopic corrections (F_s in Equation 1, green), H2O-related corrections ($M_v \cdot F_{d,v}$ in Equation 2, red), and net corrections ($F_{d,T} + F_{d,v} + F_s$ in Equation 1, black). The sample sizes for the corresponding hour are shown in (e) and (f), repsectively

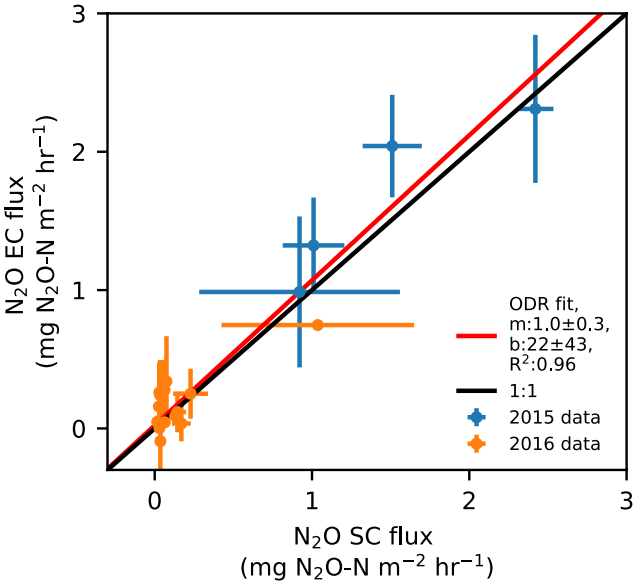


FIGURE 4 Comparison between eddy covariance (EC) and static chamber (SC) N_2O fluxes ($n = 18$). Vertical error bars show the standard deviation of EC observations made ±2 h of the SC measurement time. Horizontal error bars show the standard deviation of SC measurements made at different locations of the field. The red line shows error-weighted orthogonal distance regression (ODR) result using both 2015 and 2016 observations. The uncertainties for the ODR results are 95% CI

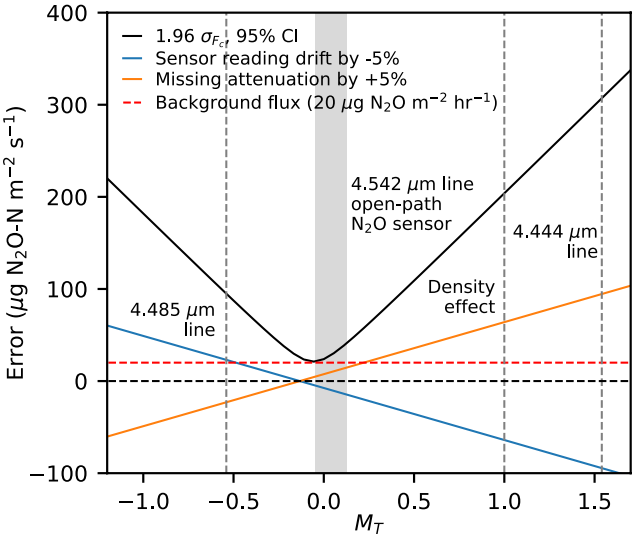


FIGURE 5 Examples of impacts of temperature multiplier (M_T) on random and systematic errors of corrected flux with a sensible heat flux of 200 W m^{-2} s^{-1}, a latent heat flux of 200 W m^{-2} s^{-1}, an ambient pressure of 101 kPa, an ambient temperature of 25°C, and N_2O concentration of 310 ppbv. The random error (the solid black line, $1.96\sigma F_c$, 95% CI) of the corrected flux are square roots of the sum of random errors of measured flux and correction terms. The blue and orange lines represent systematic errors associated with sensor drifting (−5%) and over-correction of high-frequency attenuation for correction terms (+5%), respectively. The dash grey lines show the M_T for the 4.485 μm N_2O line, pure density effect ($M_T = 1$), and the 4.444 μm N_2O line. The grey area shows the measured M_T during the field tests in 2015 and 2016 using the 4.542 μm N_2O line

3.2 | Measured density and spectroscopic corrections

Relatively small corrections (diel mean values about 70 μg N_2O-N m^{-2} h^{-1} in both 2015 and 2016) are needed when using the open-path N_2O sensor to measure EC fluxes, as demonstrated by the diel patterns and means of raw N_2O fluxes ($\overline{w'\rho'_{cm}}$) and corrected N_2O fluxes in Figure 3 and Table 3. Figure 3 also shows spectroscopic and density corrections for EC flux measurements. Both corrections were comparable to the observed N_2O fluxes, especially during the day when sensible heat and latent heat fluxes were large. However, spectroscopic and density corrections canceled each other as expected, with the net corrections at one-third of density corrections on average. Noteworthily, the changes in temperature, pressure, and H_2O concentrations introduce variations to M_T, which varied from −0.05 to 0.13 during the field tests for the open-path N_2O sensor using the 4.542 μm line. Even considering these variations, the net temperature-related correction will remain small if $|M_T|$ is minimized for the targeted temperature. Only 20% of the net corrections were caused by temperature-related effects based on fluxes and corrections calculated using Equation (2), which were ~6% of density corrections.

Unlike the temperature-related spectroscopic effect, the H_2O-induced spectroscopic effect impacts the reading in the same direction as the H_2O dilution effect. As a result, M_v cannot be minimized the same way as M_T, and H_2O-related effects require large corrections (Table 1). As shown in Figure 3c,d, the H_2O-related correction dominates the overall correction when the temperature-related correction is minimized. Measuring H_2O by simultaneously scanning both target gas and H_2O using the same instrument instead of using H_2O concentrations measured by a different sensor (often in a different location) can reduce the errors. For example, the 4.546 μm N_2O line has an adjacent H_2O line that could be used for H_2O corrections. We did not use this line in the field as the QCL tuning range was insufficient for our tests. Nonetheless, any H_2O measurements would also be impacted by spectroscopic and density effects, as shown in Table 2. Although $|M_T|$ for these adjacent H_2O lines is larger than those of the desired CO_2, CH_4, and N_2O lines, $F_{d,T}$ of H_2O flux is relatively small compared to typical H_2O fluxes. Therefore, temperature-related spectroscopic and density effects have limited impacts on these adjacent H_2O lines.

3.3 | Random and systematic errors caused by corrections

With the new QCL-based, open-path N_2O sensor, the observed net corrections had much smaller variations than spectroscopic and density corrections because they canceled each other (Figure 3c,d). These results are consistent with Equation (4) for near-zero $|M_T|$. Figure 5 further illustrates the effects of minimizing $|M_T|$ on EC flux errors. Background-level flux (20 μg N_2O-N m^{-2} h^{-1}) is considered with the same $F_{d,T}$ as listed in Table 2 and an $F_{d,v}$ of 150 μg N_2O-N m^{-2} h^{-1} (LE~200 W m^{-2} s^{-1}).

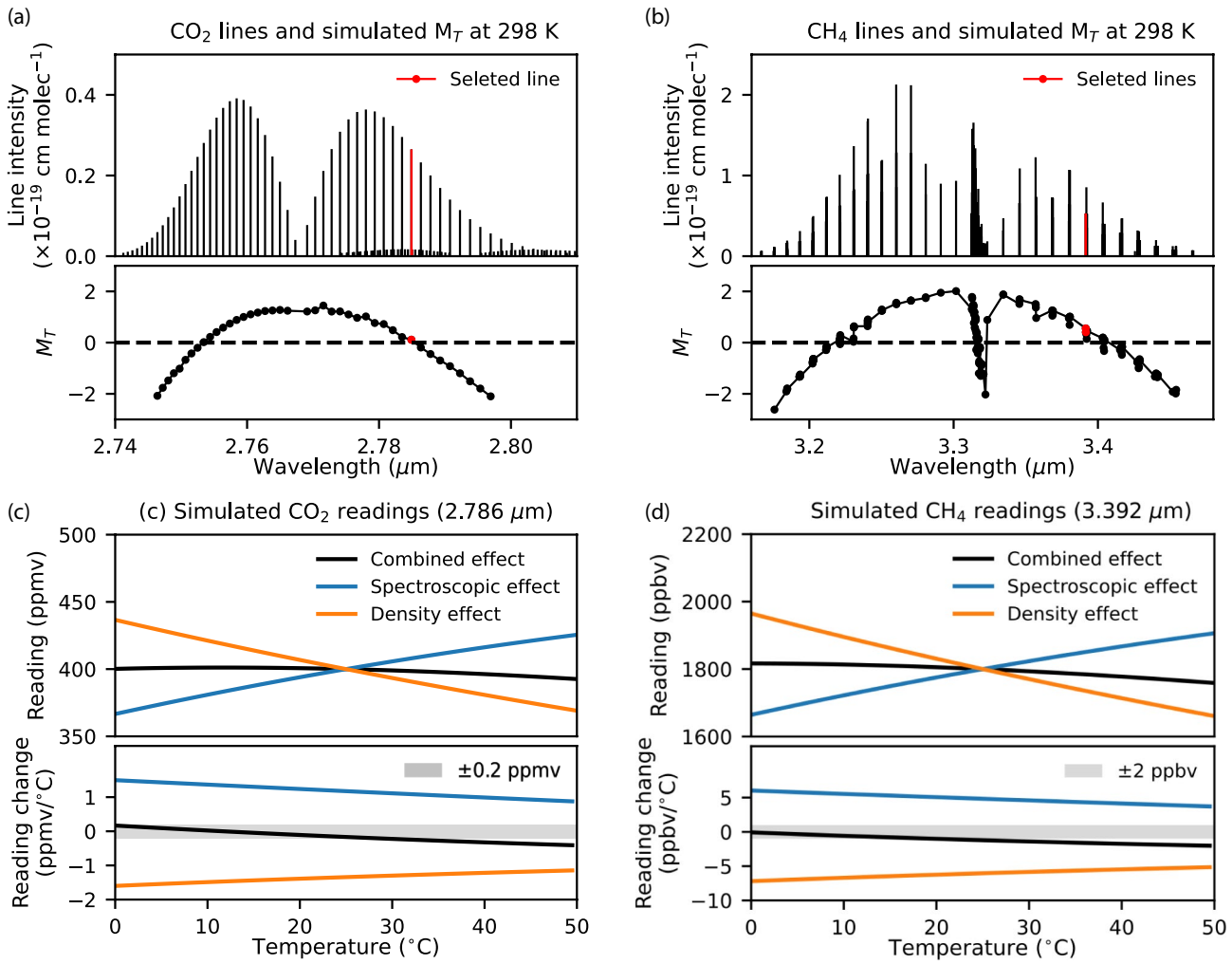


FIGURE 6 Line intensities, simulated values of temperature multiplier (M_T), and simulated temperature impacts on sensor readings for CO_2 and CH_4 lines near 2.77 and 3.3 μm, respectively. Panels (a) and (b) show line intensities and M_T for CO_2 and CH_4 lines. Red lines and dots show selected lines for detailed sensor performance simulations at 2.786 and 3.392 μm. Panels (c) and (d) show simulated temperature impacts on sensor readings for 400 ppmv CO_2 and 1800 ppbv CH_4 using the selected CO_2 and CH_4 lines, respectively

Random and systematic errors are considered. Random error calculated using Equation (4) with $\overline{w'\rho'_{cm}}$, $\overline{w'T'}$, and $\overline{w'\rho'_v}$ assumed to have a relative uncertainty of 15% (95% CI). The minimal random error of the corrected flux occurs at M_T close to zero, which is 10 and 15 times smaller than the random errors at $M_T = 1$ (density effects only) and $M_T = 1.54$ (4.444 μm N_2O line), respectively. Systematic errors, including a −5% bias because of sensor reading drift and +5% biases in $F_{d,T}$ and $F_{d,v}$ terms due to frequency-response correction errors, are also minimized when M_T approaches 0 (Figure 5). Systematic biases in $F_{d,T}$ and $F_{d,v}$ frequently occur as there are larger uncertainties in frequency-response corrections for path-averaging and sensor separations (Burba et al., 2019).

Random and systematic errors illustrated here are idealized and simplified. Previous EC calculations estimated the random error of corrected flux by assuming it has the same relative magnitude of $\sigma_{\overline{w'\rho'_{cm}}}$ (Mauder et al., 2013). Compared to Equation (4), the conventional way could significantly underestimate the random error as strong density and spectroscopic effects increase the apparent signal-to-noise ratio (see SI Section V for more details). Using Equation (4) considers the errors propagated through corrections, but it assumes that random errors of $\overline{w'\rho'_{cm}}$, $\overline{w'\rho'_v}$, and $\overline{w'T'}$ are independent of each other, which needs further investigation. Moreover, other systematic errors could exist in sensible heat and latent heat fluxes, as widely shown by energy closure issues (Lee & Massman, 2011; Richardson et al., 2006). Nevertheless, having a $|M_T|$ that minimizes the errors propagated through corrections reduces uncertainties in corrected fluxes and increases the confidence in EC flux measurements.

3.4 | Implications for flux measurements

With the conventional line selection, N_2O EC fluxes measured by an open-path sensor would be overwhelmed by spectroscopic and

density corrections. Using the method proposed here, however, we minimize the net temperature-related corrections for EC measurements, making it possible to measure background N_2O flux. We developed a laser-based, open-path N_2O and conducted the first open-path N_2O EC flux measurements powered by solar panels. We show that the net temperature-related corrections were significantly reduced, and corrected fluxes were in close agreement with conventional static chamber-based fluxes over the same periods (Figure 4).

More broadly, values of M_T at 0, 25, and 50°C were calculated for CO_2 lines near 1.6 and 2.7 μm, CH_4 lines near 1.6 and 3.3 μm, and H_2O lines adjacent to the CO_2 and CH_4 lines investigated. We identified CO_2 and CH_4 lines that have near-zero $|M_T|$ and can significantly reduce the net temperature-related correction (Table 1). The lines listed in Burba et al. (2019) are also included in Table 2 for comparison, and the same sensible heat flux, gas fluxes, and $F_{d,T}$ used in their study were used to estimate correction terms and their contributions to total fluxes. Figure 6 shows examples of selected CO_2 and CH_4 lines. For CO_2, the potential lines identified in our method reduces the net temperature-related correction by up to 100 times at 25°C compared to an NDIR sensor (e.g., LI-7500 CO_2/H_2O analyzer) which has an $M_T = 1$. For CH_4, the potential lines can reduce the temperature-related correction by about ten times compared to existing commercially available open-path CH_4 instruments at 25°C. $|M_T|$ remains relatively small for these lines when temperature changes from 0 to 50°C (<0.34). Although detailed laboratory validation and field tests are still needed for CO_2 and CH_4 lines, our work provides a new direction for future low-power and easy-to-use instruments for flux measurements.

ACKNOWLEDGMENTS

M.A.Z and I.G. acknowledge support from NSF DEB-1359538 for field measurements at KBS. M.A.Z. also acknowledges support from DOE DE-SC0011288 for sensor development. We appreciate the support of staff and resources at KBS for the assistance of field measurements. Support for this research was provided by the Great Lakes Bioenergy Research Center, U.S. Department of Energy, Office of Science, Office of Biological and Environmental Research (Award DE-SC0018409), by the National Science Foundation Long-term Ecological Research Program (DEB 1832042) at the Kellogg Biological Station, and by Michigan State University AgBioResearch. We appreciate the helpful discussion with Professor Elie Bou-Zeid.

CONFLICT OF INTEREST

The authors declare no competing financial interest.

DATA AVAILABILITY STATEMENT

The spectroscopic results and 30-min flux data that support the findings of this study are openly available in DataSpace at Princeton University at https://doi.org/10.34770/ensr-9q19. The 10-Hz raw eddy covariance data is available at http://arks.princeton.edu/ark:/88435/dsp01dn39x467g.

ORCID

Da Pan https://orcid.org/0000-0002-1618-7389
Ilya Gelfand https://orcid.org/0000-0002-8576-0978
Lei Tao https://orcid.org/0000-0001-6901-9525
Michael Abraha https://orcid.org/0000-0001-8952-9477
Kang Sun https://orcid.org/0000-0002-9930-7509
Xuehui Guo https://orcid.org/0000-0002-6983-6856
Jiquan Chen https://orcid.org/0000-0003-0761-9458
G. Philip Robertson https://orcid.org/0000-0001-9771-9895
Mark A. Zondlo https://orcid.org/0000-0003-2302-9554

REFERENCES

Abraha, M., Hamilton, S. K., Chen, J., & Robertson, G. P. (2018). Ecosystem carbon exchange on conversion of Conservation Reserve Program grasslands to annual and perennial cropping systems. *Agricultural and Forest Meteorology*, *253*, 151–160. https://doi.org/10.1016/j.agrformet.2018.02.016

Anderson, D. E., Verma, S. B., & Rosenberg, N. J. (1984). Eddy correlation measurements of CO_2, latent heat, and sensible heat fluxes over a crop surface. *Boundary-Layer Meteorology*, *29*(3), 263–272. https://doi.org/10.1007/BF00119792

Auble, D. L., & Meyers, T. P. (1992). An open path, fast response infrared absorption gas analyzer for H_2O and CO_2. *Boundary-Layer Meteorology*, *59*(3), 243–256. https://doi.org/10.1007/BF00119815

Baldocchi, D. D. (2020). How eddy covariance flux measurements have contributed to our understanding of global change biology. *Global Change Biology*, *26*(1), 242–260.

Baldocchi, D., Falge, E., Gu, L., Olson, R., Hollinger, D., Running, S., Anthoni, P., Bernhofer, C. H., Davis, K., Evans, R., Fuentes, J., Goldstein, A., Katul, G., Law, B., Lee, X., Malhi, Y., Meyers, T., Munger, W., Oechel, W., … Wofsy, S. (2001). FLUXNET: A new tool to study the temporal and spatial variability of ecosystem-scale carbon dioxide, water vapor, and energy flux densities. *Bulletin of the American Meteorological Society*, *82*(11), 2415–2434. https://doi.org/10.1175/1520-0477(2001)082<2415:FANTTS>2.3.CO;2

Burba, G., Anderson, T., & Komissarov, A. (2019). Accounting for spectroscopic effects in laser-based open-path eddy covariance flux measurements. *Global Change Biology*, *25*(6), 2189–2202. https://doi.org/10.1111/gcb.14614

Burba, G., McDermitt, D., Anderson, D., Furtaw, M., & Eckles, R. (2010). Novel design of an enclosed CO_2/H_2O gas analyser for eddy covariance flux measurements. *Tellus B: Chemical and Physical Meteorology*, *62*(5), 743–748.

Chamberlain, S. D., Verfaillie, J., Eichelmann, E., Hemes, K. S., & Baldocchi, D. D. (2017). Evaluation of density corrections to methane fluxes measured by open-path eddy covariance over contrasting landscapes. *Boundary-Layer Meteorology*, *165*(2), 197–210. https://doi.org/10.1007/s10546-017-0275-9

Eugster, W., & Plüss, P. (2010). A fault-tolerant eddy covariance system for measuring CH_4 fluxes. *Agricultural and Forest Meteorology*, *150*(6), 841–851. https://doi.org/10.1016/j.agrformet.2009.12.008

Goulden, M. L., Munger, J. W., Fan, S. M., Daube, B. C., & Wofsy, S. C. (1996). Measurements of carbon sequestration by long-term eddy covariance: Methods and a critical evaluation of accuracy. *Global Change Biology*, *2*(3), 169–182. https://doi.org/10.1111/j.1365-2486.1996.tb00070.x

Ham, J., & Heilman, J. (2003). Experimental test of density and energy-balance corrections on carbon dioxide flux as measured using open-path eddy covariance. *Agronomy Journal*, *95*(6), 1393–1403. https://doi.org/10.2134/agronj2003.1393

Hanson, R. K., Spearrin, R. M., & Goldenstein, C. S. (2016). *Spectroscopy and optical diagnostics for gases*. Springer.

Holland, E. A., Robertson, G. P., Greenberg, J., Groffman, P. M., Boone, R. D., & Gosz, J. R. (1999). Soil CO_2, N_2O, and CH_4 exchange. In G. P. Robertson, D. C. Coleman, C. S. Bledsoe, & P. Sollins (Eds.), *Standard soil methods for long-term ecological research* (pp. 185–201). Oxford University Press.

Huang, H., Wang, J., Hui, D., Miller, D. R., Bhattarai, S., Dennis, S., & Reddy, K. C. (2014). Nitrous oxide emissions from a commercial cornfield (*Zea mays*) measured using the eddy covariance technique. *Atmospheric Chemistry and Physics*, *14*(23), 12839–12854. https://doi.org/10.5194/acp-14-12839-2014

Kroon, P., Hensen, A., Jonker, H., Ouwersloot, H., Vermeulen, A., & Bosveld, F. (2010). Uncertainties in eddy covariance flux measurements assessed from CH_4 and N_2O observations. *Agricultural and Forest Meteorology*, *150*(6), 806–816. https://doi.org/10.1016/j.agrformet.2009.08.008

Kroon, P. S., Hensen, A., Jonker, H. J. J., Zahniser, M. S., van 't Veen, W. H., & Vermeulen, A. T. (2007). Suitability of quantum cascade laser spectroscopy for CH_4 and N_2O eddy covariance flux measurements. *Biogeosciences*, *4*, 715–728. https://doi.org/10.5194/bg-4-715-2007

Lee, X., & Massman, W. J. (2011). A perspective on thirty years of the Webb, Pearman and Leuning density corrections. *Boundary-Layer Meteorology*, *139*(1), 37–59. https://doi.org/10.1007/s10546-010-9575-z

Leuning, R., Denmead, O., Lang, A., & Ohtaki, E. (1982). Effects of heat and water vapor transport on eddy covariance measurement of CO_2 fluxes. *Boundary-Layer Meteorology*, *23*(2), 209–222. https://doi.org/10.1007/BF00123298

Mastepanov, M., Sigsgaard, C., Dlugokencky, E. J., Houweling, S., Ström, L., Tamstorf, M. P., & Christensen, T. R. (2008). Large tundra methane burst during onset of freezing. *Nature*, *456*(7222), 628–630. https://doi.org/10.1038/nature07464

Mauder, M., Cuntz, M., Drüe, C., Graf, A., Rebmann, C., Schmid, H. P., Schmidt, M., & Steinbrecher, R. (2013). A strategy for quality and uncertainty assessment of long-term eddy-covariance measurements. *Agricultural and Forest Meteorology*, *169*, 122–135. https://doi.org/10.1016/j.agrformet.2012.09.006

McDermitt, D., Burba, G., Xu, L., Anderson, T., Komissarov, A., Riensche, B., Schedlbauer, J., Starr, G., Zona, D., Oechel, W., Oberbauer, S., & Hastings, S. (2011). A new low-power, open-path instrument for measuring methane flux by eddy covariance. *Applied Physics B*, *102*(2), 391–405. https://doi.org/10.1007/s00340-010-4307-0

Montzka, S. A., Dlugokencky, E. J., & Butler, J. H. (2011). Non-CO_2 greenhouse gases and climate change. *Nature*, *476*(7358), 43–50.

Nakai, T., Hiyama, T., Petrov, R. E., Kotani, A., Ohta, T., & Maximov, T. C. (2020). Application of an open-path eddy covariance methane flux measurement system to a larch forest in eastern Siberia. *Agricultural and Forest Meteorology*, *282*, 107860. https://doi.org/10.1016/j.agrformet.2019.107860

Neftel, A., Ammann, C., Fischer, C., Spirig, C., Conen, F., Emmenegger, L., Tuzson, B., & Wahlen, S. (2010). N_2O exchange over managed grassland: Application of a quantum cascade laser spectrometer for micrometeorological flux measurements. *Agricultural and Forest Meteorology*, *150*(6), 775–785. https://doi.org/10.1016/j.agrformet.2009.07.013

Nemitz, E., Mammarella, I., Ibrom, A., Aurela, M., Burba, G. G., Dengel, S., Gielen, B., Grelle, A., Heinesch, B., Herbst, M., Hörtnagl, L., Klemedtsson, L., Lindroth, A., Lohila, A., McDermitt, D. K., Meier, P., Merbold, L., Nelson, D., Nicolini, G., … Zahniser, M. (2018). Standardisation of eddy-covariance flux measurements of methane and nitrous oxide. *International Agrophysics*, *32*(4). https://doi.org/10.1515/intag-2017-0042

Oates, L. G., Duncan, D. S., Gelfand, I., Millar, N., Robertson, G. P., & Jackson, R. D. (2016). Nitrous oxide emissions during establishment of eight alternative cellulosic bioenergy cropping systems in the North Central United States. *GCB Bioenergy*, *8*(3), 539–549. https://doi.org/10.1111/gcbb.12268

Richardson, A. D., Hollinger, D. Y., Burba, G. G., Davis, K. J., Flanagan, L. B., Katul, G. G., William Munger, J., Ricciuto, D. M., Stoy, P. C., Suyker, A. E., Verma, S. B., & Wofsy, S. C. (2006). A multi-site analysis of random error in tower-based measurements of carbon and energy fluxes. *Agricultural and Forest Meteorology*, *136*(1–2), 1–18. https://doi.org/10.1016/j.agrformet.2006.01.007

Tao, L., Sun, K., Khan, M. A., Miller, D. J., & Zondlo, M. A. (2012). Compact and portable open-path sensor for simultaneous measurements of atmospheric N_2O and CO using a quantum cascade laser. *Optics Express*, *20*(27), 28106–28118.

Wang, K., Zheng, X., Pihlatie, M., Vesala, T., Liu, C., Haapanala, S., Mammarella, I., Rannik, Ü., & Liu, H. (2013). Comparison between static chamber and tunable diode laser-based eddy covariance techniques for measuring nitrous oxide fluxes from a cotton field. *Agricultural and Forest Meteorology*, *171*, 9–19. https://doi.org/10.1016/j.agrformet.2012.11.009

Webb, E. K., Pearman, G. I., & Leuning, R. (1980). Correction of flux measurements for density effects due to heat and water vapour transfer. *Quarterly Journal of the Royal Meteorological Society*, *106*(447), 85–100. https://doi.org/10.1002/qj.49710644707

Zenone, T., Zona, D., Gelfand, I., Gielen, B., Camino-Serrano, M., & Ceulemans, R. (2016). CO_2 uptake is offset by CH_4 and N_2O emissions in a poplar short-rotation coppice. *GCB Bioenergy*, *8*(3), 524–538.

Zhang, J., Lee, X., Song, G., & Han, S. (2011). Pressure correction to the long-term measurement of carbon dioxide flux. *Agricultural and Forest Meteorology*, *151*(1), 70–77. https://doi.org/10.1016/j.agrformet.2010.09.004

Zona, D., Janssens, I., Aubinet, M., Gioli, B., Vicca, S., Fichot, R., & Ceulemans, R. (2013a). Fluxes of the greenhouse gases (CO_2, CH_4 and N_2O) above a short-rotation poplar plantation after conversion from agricultural land. *Agricultural and Forest Meteorology*, *169*, 100–110. https://doi.org/10.1016/j.agrformet.2012.10.008

Zona, D., Janssens, I. A., Gioli, B., Jungkunst, H. F., Serrano, M. C., & Ceulemans, R. (2013b). N_2O fluxes of a bio-energy poplar plantation during a two years rotation period. *GCB Bioenergy*, *5*(5), 536–547.

SUPPORTING INFORMATION

Additional supporting information may be found in the online version of the article at the publisher's website.

How to cite this article: Pan, D., Gelfand, I., Tao, L., Abraha, M., Sun, K., Guo, X., Chen, J., Robertson, G. P., & Zondlo, M. A. (2022). A new open-path eddy covariance method for nitrous oxide and other trace gases that minimizes temperature corrections. *Global Change Biology*, 28, 1446–1457. https://doi.org/10.1111/gcb.15986

Supporting Information for: A New Open-Path Eddy Covariance Method for Nitrous Oxide and Other Trace Gases that Minimizes Temperature Correction

Da Pan[1,2,‡], Ilya Gelfand[3,4,5], Lei Tao[1,2], Michael Abraha[3,4,6], Kang Sun[7,8], Xuehui Guo[1,2], Jiquan Chen[3,6], G. Philip Robertson[3,4,9], Mark A. Zondlo[1,2,*]

[1] Department of Civil and Environmental Engineering, Princeton University, Princeton, New Jersey 08544, United States of America

[2] Center for Mid-Infrared Technologies for Health and the Environmental, NSF-ERC, Princeton, New Jersey 08544, United States of Americas

[3] Great Lakes Bioenergy Research Center, Michigan State University, East Lansing, Michigan 48824, United States of America

[4] W.K. Kellogg Biological Station, Michigan State University, Hickory Corners, Michigan 49060, United States of America

[5] The French Associates Institute for Agriculture and Biotechnology of Drylands, The Jacob Blaustein Institutes for Desert Research, Ben-Gurion University of the Negev, Beer-Sheva 84990, Israel

[6] Center for Global Change and Earth Observations, Michigan State University, East Lansing, Michigan 48823, United States of America

[7] Department of Civil, Structural and Environmental Engineering, University at Buffalo, Buffalo, New York 14260, United States of America

[8] Research and Education in eNergy, Environment and Water (RENEW) Institute, University at Buffalo, Buffalo, New York 14260, United States of America

[9] Department of Plant, Soil, and Microbial Sciences, Michigan State University, East Lansing, Michigan 48824, United States of America

‡ Now at Department of Atmospheric Science, Colorado State University, Fort Collins, CO, 80525, United States of America

* To whom correspondence may be addressed. Email: mzondlo@princeton.edu

Table of Contents

I. Spectroscopic calculation 3

II. Measurements of water-vapor broadened half-width at half-maximum (HWHM) 6

III. Validation of spectroscopic simulations 10

IV. Calibration and in-field performance of the open-path N_2O sensor 11

V. Calculation of EC flux and random errors 15

VI. SC flux measurements and uncertainty estimates for SC and EC comparison 19

VII. Measured EC fluxes 21

VIII. Flux random errors and detection limits 26

IX. Cospectra and high-frequency attenuation 27

X. Comparisons between SC and EC fluxes with time windows of ±1 hour and ±3 hours 28

Supplementary references 29

I. Spectroscopic calculation

The HITRAN Application Programming Interface (HAPI) was used to calculate the line intensity and line shape at a given temperature and pressure (Kochanov et al., 2016). The absorption of an absorption line centered at ν'' at wavenumber ν (cm^{-1}) can be calculated as

$$1 - \frac{I}{I_0} = \exp(-nS(T)f(\nu;\nu'',T,p)L) \tag{S1}$$

where I is the light intensity passing through the sample cell; I_0 is the original light intensity; n is number density of target gas in the sample cell; $S(T)$ is the line intensity; $f(\nu;\nu'',T,p)$ is the line shape function; and L is the length of the sample cell.

The line intensity can be calculated as

$$S(T) = S(T_{\mathrm{ref}})\frac{Q(T_{\mathrm{ref}})}{Q(T)}\frac{\exp(-c_2E''/T)}{\exp(-c_2E''/T_{\mathrm{ref}})}\frac{[1-\exp(c_2\nu/T)]}{[1-\exp(c_2\nu/T_{\mathrm{ref}})]} \tag{S2}$$

where S is the line intensity (cm^{-1} molecule^{-1} cm^{-2}), Q is the total internal partition sum, T_{ref} equals to 296 K, T is the ambient temperature (K), c_2 is the second radiation constant, E'' is the lower-state energy of the transition line (cm^{-1}), and ν is the wavenumber of transition line (cm^{-1}). The line shape also changes with temperature and pressure. The Voigt line shape is used in this study, which is a convolution of a Gaussian profile (Doppler-broadening effect) and a Lorentzian profile (pressure-broadening effect). The half-width at half-maximum (HWHM) of the Gaussian profile is given by

$$\alpha_D(T) = \frac{\nu}{c}\sqrt{\frac{2N_AkT\ln 2}{M}} \tag{S3}$$

where α_D is the HWHM of the Gaussian profile in cm^{-1}, c is the speed of light (cm s^{-1}), N_A is the Avogadro constant, k is the Boltzmann constant, and M is the molar mass of the target gas. The Lorentzian HWHM is calculated as

$$\gamma(p,T) = \left(\frac{T_{\mathrm{ref}}}{T}\right)^{n_{\mathrm{air}}}\gamma_{\mathrm{air}}\left(p_{\mathrm{dryair}} + \frac{\gamma_{\mathrm{H_2O}}}{\gamma_{\mathrm{air}}}e\right) = \left(\frac{T_{\mathrm{ref}}}{T}\right)^{n_{\mathrm{air}}}\gamma_{\mathrm{air}}p_e \tag{S4}$$

where γ is the Lorentzian HWHM (cm^{-1}), n_{air} is the coefficient of the temperature dependence of the air-broadened half-width, γ_{air} is the air-broadened HWHM (cm^{-1}/atm) at 296 K and 1 atm, p_{dryair} is the pressure of dry air (atm), $\gamma_{\mathrm{H_2O}}$ is the water vapor-broadened HWHM (cm^{-1}/atm) at 296 K and 1 atm, e is water vapor pressure (atm), and p_e is the effective pressure (atm). The self-broadening effect is ignored here. The Gaussian profile can be expressed as

$$f_G(\nu;\nu'',T) = \sqrt{\frac{\ln 2}{\pi\,\alpha_D^2}}\exp\left(-\frac{(\nu-\nu'')^2\ln 2}{\alpha_D^2}\right) \tag{S5}$$

The Lorentzian profile can be expressed as

$$f_L(\nu;\nu'',T,p) = \frac{1}{\pi}\frac{\gamma(p,T)}{\gamma(p,T)^2+\left[\nu-\left(\nu''+\delta_p\right)\right]^2} \tag{S6}$$

where δ_p is the pressure shift. And the Voigt profile is a convolution of the Gaussian profile and the Lorentzian profile

$$\gamma_\nu(\nu;\nu'',T,p) = \int_{-\infty}^{+\infty} f_G(\nu';\nu'',T) f_L(\nu-\nu';\nu'',T,p)\,\mathrm{d}\nu' \tag{S7}$$

The Voigt profile is calculated using HAPI (Kochanov et al., 2016).

The open-path N_2O sensor measures N_2O concentration as the peak-to-trough height (PTH) of the second harmonic (2f) signal of wavelength modulation spectroscopy (WMS). 2f signals were simulated following Sun, Tao, Miller, Khan, and Zondlo (2013). In addition to slow ramp scans across the absorption feature, a high-frequency modulation is added to drive the laser. The drive current can be expressed as

$$i(t) = i_R R(2\pi f_R t) + i_m\cos(2\pi f_m t) + \mathrm{DC} \tag{S8}$$

where i_R and i_m are the amplitudes of the current ramp and sinusoidal modulation; $R(2\pi f_R t)$ is the sawtooth ramp function with frequency f_R; and DC is the direct current component. The current modulation leads to a laser intensity modulation that is proportional to the drive current as well as a frequency modulation around ν_0, which can be expressed as

$$\nu(t) = i_R\eta_R R(2\pi f_R t) + i_m\eta_m\cos(2\pi f_m t+\phi) + \nu_0 \tag{S9}$$

where η_R and η_m are the current-to-frequency tuning rates (cm^{-1}/mA) at the ramp frequency and modulation frequency; and ϕ is the phase difference between the modulated laser frequency and laser intensity. η_R, η_m, and ϕ are experimentally measured using the method described in Tao, Sun, Khan, Miller, and Zondlo (2012).

Detector signals can be simulated by substituting Eq. (S9) in Eq. (S1). Then, an infinite impulse response (IIR) low-pass Butterworth filter ("scipy.signal.butter" function from the Scipy package) is applied to acquire WMS 2f signals, which can be expressed as

$$X(t) = \mathrm{IIR}(I(t)\cos(4\pi f_m t)) \tag{S10}$$

More details of the WMS simulation are given in Sun et al. (2013).

Simulated 2f spectra at different temperatures, pressures, and H_2O concentrations were used to derive the spectroscopic correction factor (k). k has different relationships with T, p, and ρ_v depending on the methods used to retrieve concentrations even with the same spectrum. Figure S1a shows three methods: 1) the peak-to-trough height (PTH) method normalized by the first harmonic (1f) signal; 2) the peak height method (2f peak) normalized by the 1f signal; and 3) the singular value decomposition fitting method. Figure S1b shows their response to the modulation index ($m = i_m\eta_m$/HWHM), which changes with the ambient pressure and temperature. The three approaches have different responses to temperature fluctuation, and the PTH method is used in this study.

The uncertainty (95% confidence interval (CI)) of k comes from the total internal partition sums (<1% uncertainty at 296 K; Gamache, Hawkins, & Rothman, 1990), the air-broadened half-width at half maximum (HWHM, 2% uncertainty; Gordon et al., 2017), the water-vapor broadened HWHM (10% uncertainty for the selected N_2O line, measured in this study, see SI Section III). Altogether, the uncertainty for k is relatively small compared to uncertainties in the EC method.

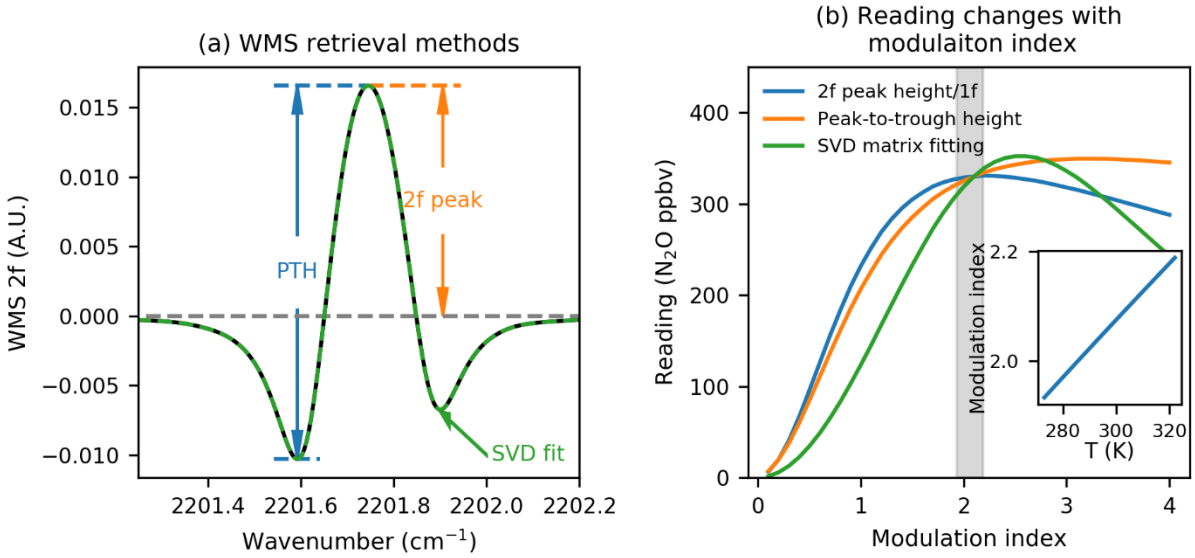


Figure S1. *Examples of different methods to retrieve the concentration from a wavelength modulation spectroscopy (WMS) 2f spectrum and their response to modulation index changes. Panel (a) shows the three approaches of retrieving the concentrations from a WMS 2f spectrum. Panel (b) shows their response to modulation index changes. The inset in panel (b) shows the relationship between modulation index and temperature at a constant pressure. The grey area in panel (b) shows the range of modulation indices when temperature changes from 0 to 50 ℃ while the pressure remains constant.*

II. Measurements of water-vapor broadened half-width at half-maximum (HWHM)

Water vapor is highly variable in the atmosphere and is a very efficient broadener of spectral lines for other gases. Therefore, changes in water vapor concentrations can lead to significant variations in retrieved N_2O concentrations. Water-vapor broadening parameters (γ_{H_2O}) for several trace gases were recently included in the HITRAN database. However, γ_{H_2O} for CO_2 was scaled to approximate γ_{H_2O} for N_2O because of limited quantification for water-vapor broadening effects on N_2O lines (Deng et al., 2017;

Tan, Kochanov, Rothman, & Gordon, 2019). To reduce the uncertainty associated with γ_{H_2O} in this study, we measured γ_{H_2O} for the P(24) N_2O line at 4.542 µm.

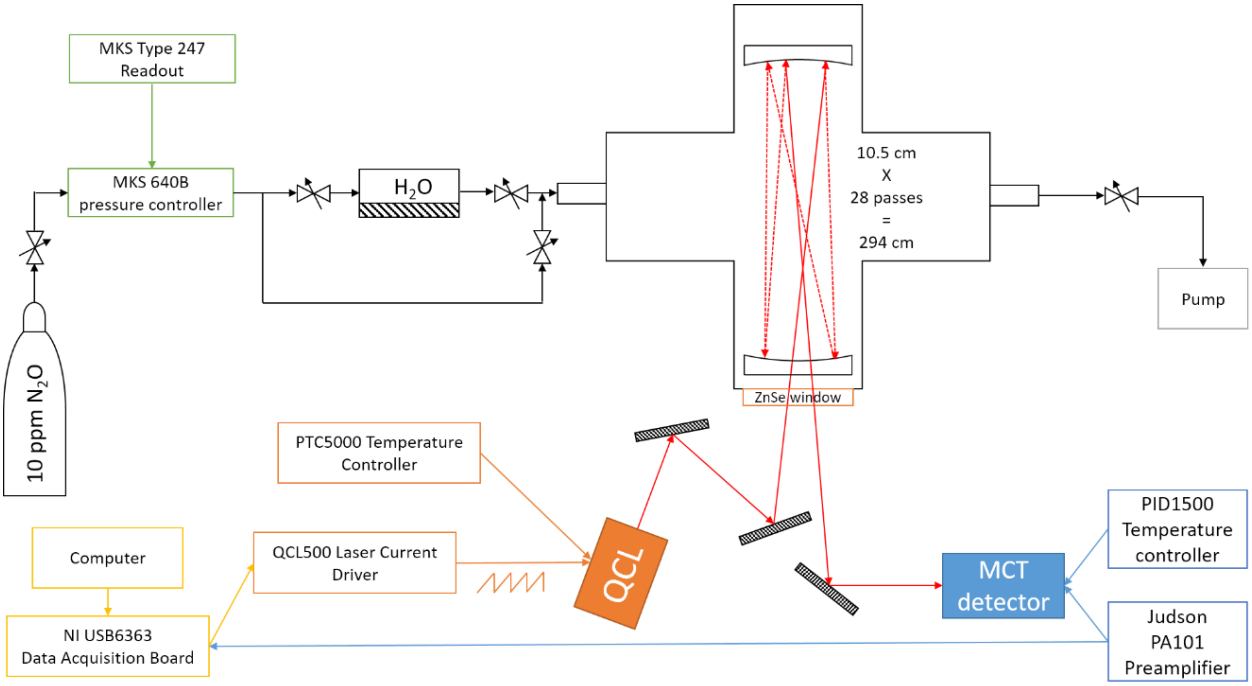


Figure S2. *Experimental setup of the γ_{H_2O} measurement. In this experiment, a QCL (Thorlabs, Inc., New Jersey, USA) was used to scan H_2O and N_2O lines from 2200 cm^{-1} to 2203 cm^{-1}. The signal was received by a MCT detector (Intelligent Materials Solutions, Inc., New Jersey, USA). The beam was directed to a 294 cm Herriot cell placed in a pressurized cell. The pressure inside the cell was controlled by an MKS 640B pressure controller (MKS Instruments, Inc., Massachusetts, USA).*

Figure S2 shows a diagram of the experiment setup. A QCL (Thorlabs, Inc., New Jersey, USA) was tuned to scan absorbing features of the H_2O line at 4.545 µm, the P(23) N_2O line at 4.534 µm, and the P(24) N_2O line at 4.542 µm by adjusting the laser temperature (PTC5000 Temperature Cssontroller; Wavelength Electronics, Inc., Montana, USA) and the injection current (QCL500 Laser Current Driver; Wavelength Electronics Inc., Montana, USA). The tuning rate (µm mA^{-1}) was determined using the three absorption lines mentioned above. The beam was directed to a 10.5 cm Herriot cell and was reflected 28 times leading to a path length of 294 cm. The Herriot cell was pressured controlled by an MKS 640B Pressure Controller (MKS Instruments, Inc., Massachusetts, USA). The beam coming out from the Herriot cell was detected by a mercury cadmium telluride (MCT) detector (Intelligent Materials Solutions, Inc., New Jersey, USA), and the detected signals were transmitted to a data acquisition board

(NI USB6363, National Instrument, Corp., Texas, USA) for post-processing. The experiment was conducted at a constant temperature (20.5 °C) and at multiple pressures inside the cell. The cell was connected to a standard gas of 10 ppmv N_2O mixed with N_2. A cell containing 0.5 L H_2O was connected through multiple valves to the pressurized cell to create dry conditions (valve-off) and near-saturated water vapor (valve-on, ~24 hPa at 20.5 °C).

The fractional absorbance spectra were calculated by subtracting the detected signals from the laser baseline and then dividing the results by the baseline. The LMFIT Python package (Newville et al., 2016) was used to fit the spectra with the Voigt profile to determine the half-widths at half-maximum (HWHM). The weak N_2O absorption lines from P(9) transitions near the P(24) transitions in the scanned region were also fitted. Three examples of fitted spectra are shown in Fig. S3. The residual between the data and the fit was typically less than 2%. Using the observed H_2O spectra and the H_2O line intensity from HITRAN 2012 with an uncertainty of 2% to 5%, the partial pressure was estimated to be 22.1 ± 0.9 hPa.

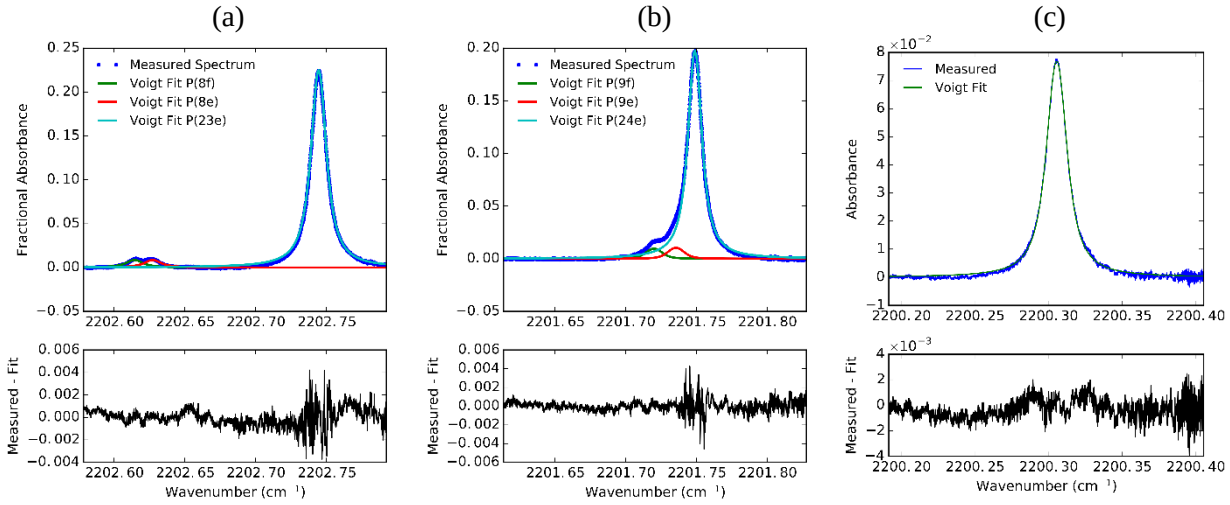


Figure S3. *Examples of fitting results for (a) the P(23) N_2O line (4.534 µm), (b) the P(24) N_2O (4.542 µm), and (c) the H_2O line (4.545 µm). The N_2O spectra were measured for 10 ppmv N_2O balanced with N_2 at 69.0 hPa. The H_2O spectrum was measured for 22.1 hPa H_2O mixed with 10 ppm N_2O balanced with N_2 at a total pressure of 69.0 hPa.*

Figure S4 shows the retrieved Lorentzian HWHMs of the P(24) N_2O line at different pressures with and without H_2O. Slopes of the regression lines were used to estimate nitrogen induced broadening

parameters γ_{H_2O}. The intercepts of L0 and L1 were used to approximate HWHMs at zero N_2 partial pressure under wet ($\mathrm{HWHM}|_{p_{N_2}=0,\mathrm{wet}}$) and dry conditions ($\mathrm{HWHM}|_{p_{N_2}=0,\mathrm{dry}}$), respectively. γ_{H_2O} was then calculated as

$$\gamma_{H_2O} = \frac{\mathrm{HWHM}|_{p_{N_2}=0,\mathrm{wet}} - \mathrm{HWHM}|_{p_{N_2}=0,\mathrm{dry}}}{p_{H_2O}} \quad \text{(S11)}$$

In the process, γ_{N_2} of the P(24) N_2O line were also determined and compared with previous studies. The uncertainty of γ_{H_2O} (95% confidence interval (CI)) can be estimated as

$$\varepsilon_{\gamma_{H_2O}} = \sqrt{\frac{\varepsilon^2_{\mathrm{HWHM}|_{p_{N_2}=0,\mathrm{wet}}} + \varepsilon^2_{\mathrm{HWHM}|_{p_{N_2}=0,\mathrm{dry}}}}{p^2_{H_2O}} + \frac{\left(\mathrm{HWHM}|_{p_{N_2}=0,\mathrm{wet}} - \mathrm{HWHM}|_{p_{N_2}=0,\mathrm{dry}}\right)^2 \varepsilon^2_{p_{H_2O}}}{p^4_{H_2O}}} \quad \text{(S12)}$$

where $\varepsilon_{\mathrm{HWHM}|_{p_{N_2}=0,\mathrm{wet}}}$ and $\varepsilon_{\mathrm{HWHM}|_{p_{N_2}=0,\mathrm{dry}}}$ are uncertainties of the intercepts derived from the regression and $\varepsilon_{p_{H_2O}}$ is the uncertainty of the water vapor partial pressure derived from the retrieval program.

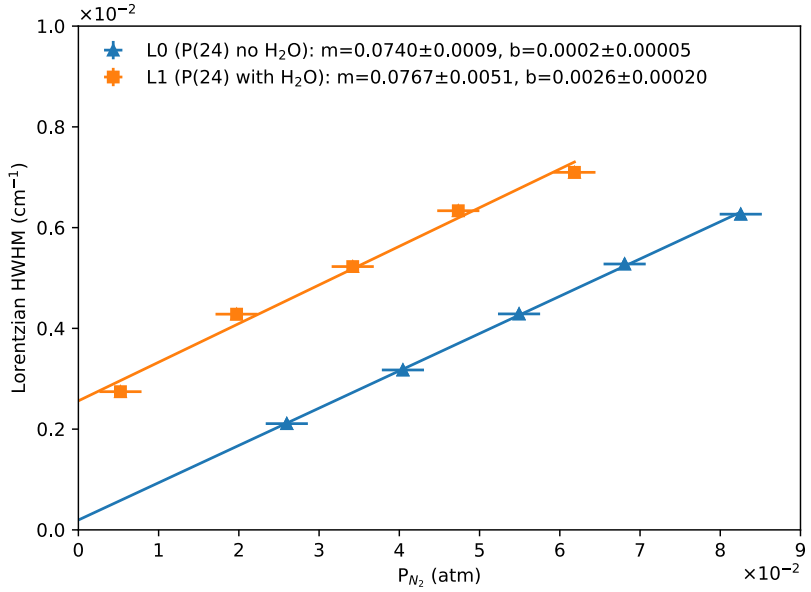


Figure S4. *Lorentzian half width at half maximum (HWHM) of the P(24) line at different pressures with (orange) and without (blue) water vapor (22.1 ± 0.9 hPa). The difference in offsets of the orange and blue lines is water-vapor broadened HWHM.*

The results are listed in Table S1. The result of γ_{N_2} is consistent with previous estimates (Lacome, Levy, & Guelachvili, 1984; Toth, 2000) and γ_{H_2O} measured in this study is 20% smaller than the estimates from HITRAN (Deng et al., 2017; Tan et al., 2019).

Table S1. Results of N_2- and H_2O-broadened line width coefficients for the P(24) line (4.542 μm, 2201.75 cm^{-1}); results from previous studies are also listed for comparison. Numbers in parentheses show 95% confidence interval.

N_2-broadened coefficient (cm^{-1} atm^{-1})			**Air-broadened coefficient (cm^{-1} atm^{-1})**	**H_2O-broadened coefficient (cm^{-1} atm^{-1})**	
Lacome et al. (1984)	Toth (2000)	This study	HITRAN (Gordon et al., 2017)	HITRAN (Tan et al., 2019)	This work
0.0754(4)	0.0756(7)	0.0754(4)	0.0730(2)	0.13(2)	0.11(1)

III. Validation of spectroscopic simulations

Figure S5 shows the schematic diagram of the experimental setup for validation of spectroscopic simulations for the 4.542 μm N_2O line. 80 ppmv N_2O mixed with N_2 was supplied to a pressure- and temperature-controlled chamber, and an optical cell with a path length of 7.62 cm was used to generate absorptions similar to those of 330 ppbv N_2O in an optical cell with a path length 1890 cm. The temperature of the chamber was controlled by a water bath and was measured by a 10-kΩ thermistor inside the chamber. The pressure of the chamber was maintained at 1.03 atm by a MKS 640B pressure controller (MKS Instruments, Inc., Massachusetts, USA). A quantum cascade laser (QCL; Hamamatsu Photonics K.K., Japan) was tuned to scan the 4.542 μm N_2O line using WMS by adjusting the laser temperature (PTC5000 Temperature Controller; Wavelength Electronics, Inc., Montana, USA) and the injection current (QCL500 Laser Current Driver; Wavelength Electronics Inc., Montana, USA). N_2O mixing ratios were measured using peak-to-trough heights (PTH) of the WMS 2f spectra and were converted to N_2O mixing ratio equivalents to a path-length of 1890 cm. The results are shown in Fig. 3c in the main text.

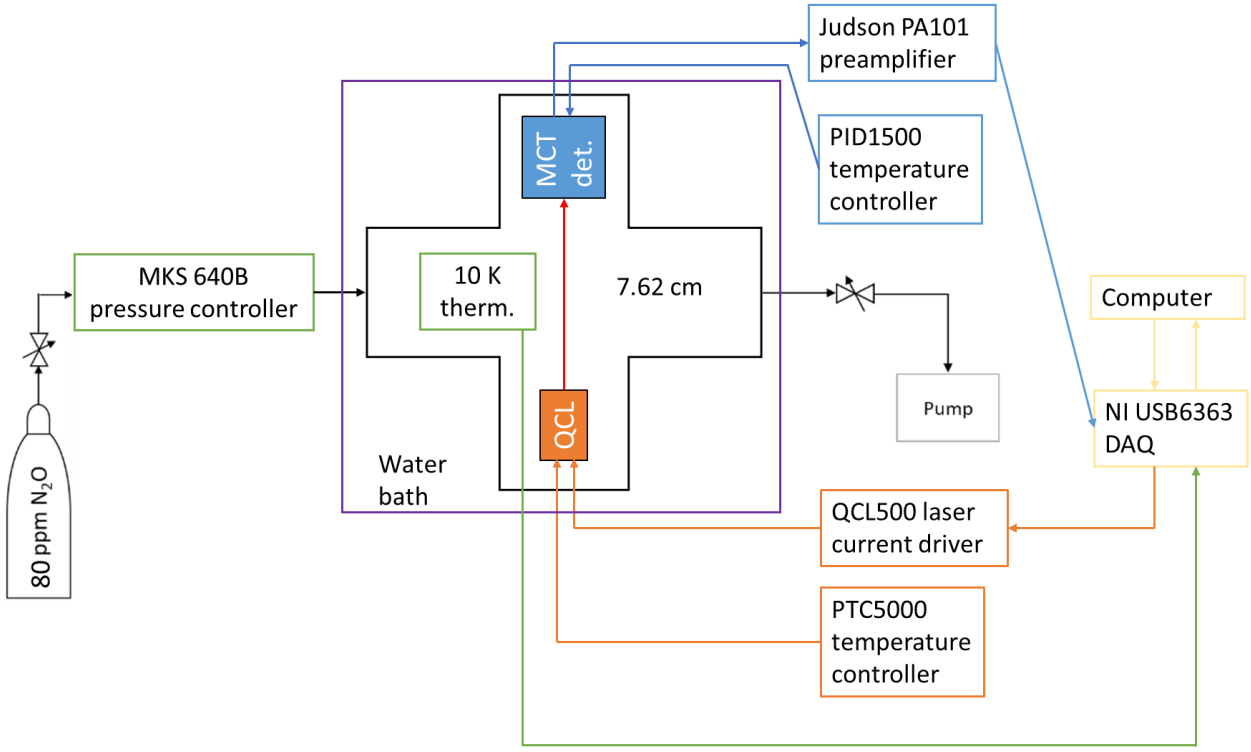


Figure S5. *Experimental setup of spectroscopic simulation validation. A quantum cascade laser (QCL; Hamamatsu Photonics K.K., Japan) was used to scan the 4.542 µm N_2O line. The signal was received by a mercury cadmium telluride (MCT) detector (Intelligent Materials Solutions, Inc., New Jersey, USA). The beam was directed to a 7.62 cm optical cell placed in a pressurized chamber. The pressure inside the cell was controlled by a MKS 640B pressure controller (MKS Instruments, Inc., Massachusetts, USA). The temperature of the chamber is controlled by a customized water bath. The temperature inside the chamber was measured by a 10k thermistor.*

IV. Calibration and in-field performance of the open-path N_2O sensor

In 2015, the N_2O sensor experienced significant drifts resulting from low-frequency optical fringes with a free spectral range (FSR) similar to the width of the N_2O absorption feature. Ranging from 5 min to a few hours depending on atmospheric conditions, drifts occurred within the average time window for EC calculation (30 min) with time scales. The drifting issue was investigated by calibrating the sensor in an environmental chamber. Figure S6 shows the calibrations of the open-path N_2O sensor that were typically conducted with three reference concentrations (0, 330, and 500 ppbv) at multiple temperatures. The error bars in Fig. S6 represent the 95% CIs of the slopes and the intercepts derived from ordinary least squares regressions between reference concentrations and sensor readings. A few calibrations were conducted with one span (0 and 500 ppbv) and, thus, have no error estimate in Fig. S6. Although the low-frequency

optical fringes were sensitive to temperature changes, the drifts did not show a statistically significant relationship with temperatures that can be used for correcting the observations. The sensitivity of the sensor, however, remained constant.

In 2016, the sensor was redesigned to improve its optomechanical stability. As a result, the drift issue was less severe in 2016, as demonstrated by calibrations in the environmental chamber similar to those of 2015 (see Fig. S6). In-field measurements in 2016 were compared with the initial concentrations of static chamber (SC) measurements calculated as the intercepts of linear regressions using four gas samples extracted from the chamber (see Fig. S7), which showed a good correlation ($R^2 = 0.61$). The observations from the open-path N_2O sensor were, in general, lower than the initial concentrations of SC measurements because the chamber measurements were closer to ground where N_2O concentrations were influenced more by the soil emissions.

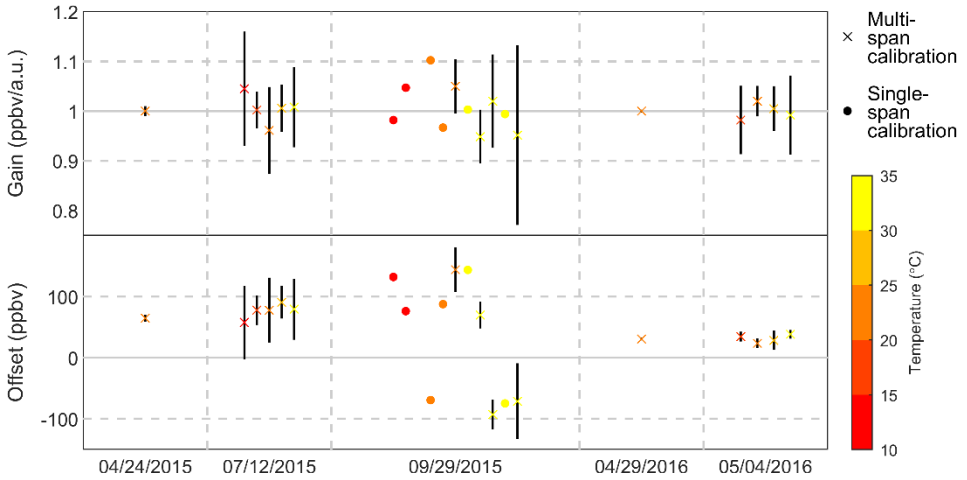


Figure S6. *Calibrations of the open-path N_2O sensor during the 2015 and 2016 field campaigns. The gains and offsets were determined using ordinary least squares regressions. The error bars show the uncertainties of the fits (95% CI). The dots are calibrations with a single span and, therefore, do not have uncertainty estimates. The calibration on 4/24/2015 and 4/29/2016 had 6 and 8 spans, respectively at constant pressure and temperature. All other calibrations were carried out in an environmental chamber that subjected to pressure changes. Calibrations in 2015 showed large drifts in the offset of the sensor.*

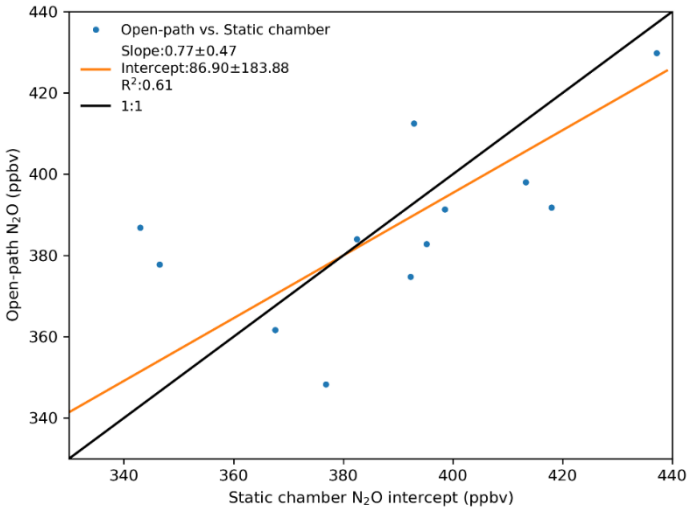


Figure S7. *Comparison between N_2O mixing ratios measured by the open-path N_2O sensor and estimated as the intercept of regressions using four gas samples from the static chamber. Orthogonal distance regression was conducted, and the uncertainties of the results are 95% confidence intervals (CIs).*

The open-path N_2O sensor was also compared with a closed-path $CH_4/N_2O/H_2O$ analyzer (Los Gatos Research (LGR) Inc., California, USA) for three days in an enclosed cabin in March 2017. The precision of N_2O measurements for the LGR N_2O analyzer was 0.2 ppbv at 1 Hz. The inlet of the LGR N_2O analyzer was placed above the center of the sampling volume of the open-path N_2O sensor. 10 ppmv N_2O was introduced initially and was naturally vented out of the cabin to create the span for comparison. Figure S8a shows the time series of N_2O concentrations measured by the open-path N_2O sensor (corrected

for spectroscopic effects, which was dominated by H_2O-related effects) and the LGR N_2O analyzer. The two instruments were synchronized by maximizing their cross-covariance. However, small discrepancies may still exist due to spatial variations of the N_2O concentration and response time differences. Overall, we found a good agreement between the two instruments for the range of 330 to 450 ppbv (Fig. S8b) with a slope of 1.00 ± 0.02 (95% CI), an intercept of 0.6 ± 0.3 ppbv, and R^2 = 0.96.

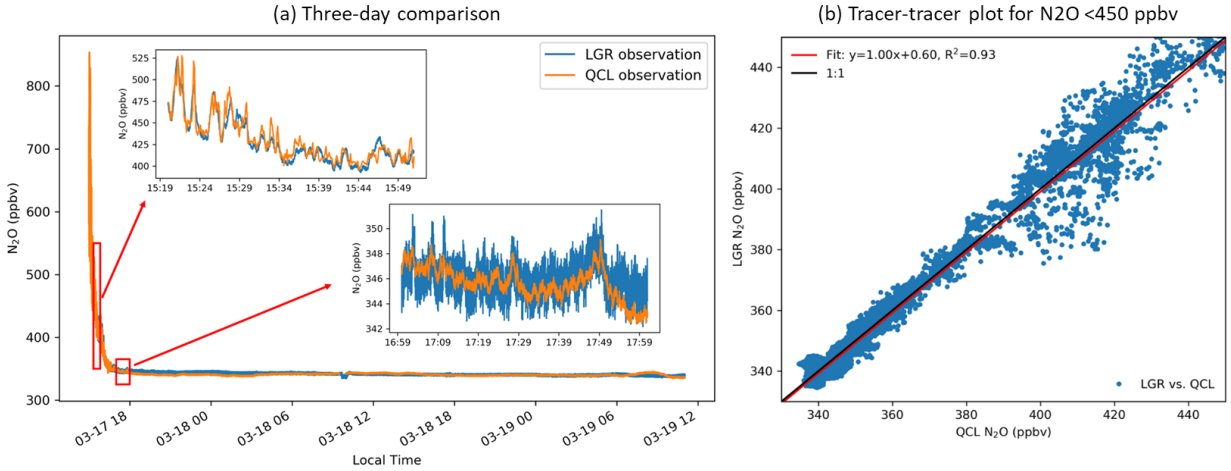


Figure S8. *Comparison between the open-path N_2O sensor and a commercial closed-path N_2O analyzer (Los Gatos Research, Inc., California, USA). (a) Time series of the three-day comparison; (b) tracer-tracer plot for N_2O concentration <450 ppbv.*

Optimal in-field precisions were estimated using observations made at the beginning of 2015 and 2016 deployments, respectively. Figure S9 shows Allan deviations of two periods with relatively stable N_2O readings. The precision of the open-path N_2O sensor was estimated to be 0.1 ppbv at 10 Hz in 2015 and 0.15 ppbv at 10 Hz in 2016. The Allan deviation increases significantly as integration time increases, reaching 0.8 ppbv at a 30-min time scale for the relatively stable period in 2015. In 2016, less drift was observed in the field. The precision of the open-path N_2O sensor worsened in 2016 because of detector and mirror deteriorations. The detector deterioration was caused by frequent shutdowns of the instrument due to insufficient power supply from solar panels. The mirror deterioration was cause by oxidation of Mo, which had not been fixed until 2019 with a new coating on the mirrors.

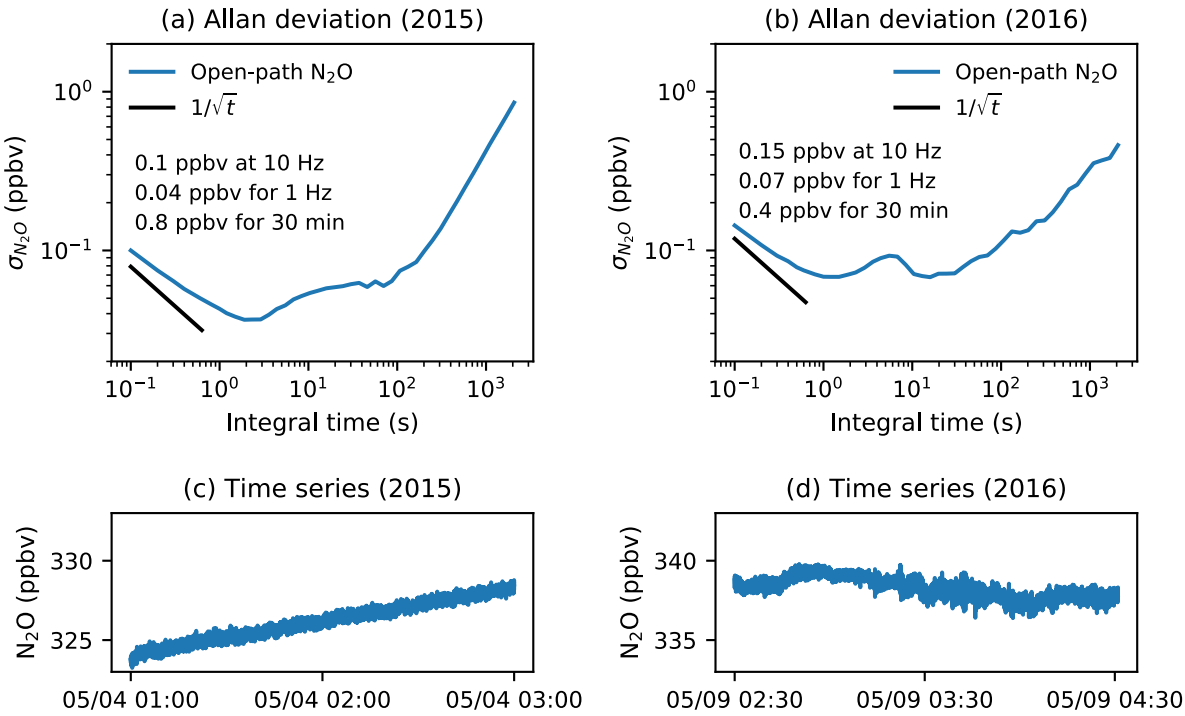


Figure S9. *Allan deviations of the open-path N_2O sensor for periods with optimal performance at the beginnings of 2015 and 2016 deployments. Panels (a) and (b) show the Allan deviations for 2015 and 2016, respectively. Panels (c) and (d) show the time series used to calculate the Allan deviations.*

V. Calculation of EC flux and random errors

Eddy covariance fluxes were calculated over 30-min intervals following the framework proposed by Mauder et al. (2013). Modifications were added to account for temperature, pressure, and water vapor spectroscopic effects on the N_2O measurements.

The first step was the post-processing of the high-frequency data, including quality control for all observations, time synchronization, spectroscopic correction for the open-path N_2O sensor, despiking (mean absolute deviation method (Mauder et al. 2013), and detrending (rolling-mean detrending with a time-window of 5 min was used in 2015 to reduce impacts of drifts, and block-average detrending was used in 2016). Temperatures and water vapor concentrations measured at 10 Hz by the sonic anemometer and the LI-7500 analyzer, respectively, were used to calculate the spectroscopic correction coefficient (k) at 10 Hz, which links measured and corrected mass density as

$$\rho_m = k(T, p, \rho_v)\rho_{cm} \quad \text{(S13)}$$

Corrections for H_2O-related effects were achieved by treating line broadening as a special case of pressure broadening (McDermitt et al., 2011). High-frequency pressure fluctuations were neglected in this study. Therefore, low-frequency pressure measurements from the LI-7500 were used for the spectroscopic correction. N_2O concentrations from the open-path N_2O sensor and H_2O measurements from the LI-7500 analyzer were adjusted for time lags with respect to the temperature measured by the anemometer due to spatial separations. The average (AVG) method proposed by Taipale, Ruuskanen, and Rinne (2010) that maximizes one second rolling average of cross-covariances within a time window of ±1.5 seconds was used for the time-lag determination. Langford, Acton, Ammann, Valach, and Nemitz (2015) showed that the AVG method could reduce the systematic biases (e.g. mirroring effects) introduced through the interplay between the sensor noise and the approach used for the time-lag determination, when compared to the cross-covariance maximization approach. The systematic biases associated with time-lag determination are of particular concerns when measured EC fluxes are near or below the flux detection limits (Langford et al., 2015).

The second step was to calculate variances and covariances, which were corrected for wind rotation (planar fit), high-frequency attenuations due to spatial separation of sensors and path length averaging (Moore, 1982), water vapor impacts on sonic temperature (SND-correction) (Liu, Peters, & Foken, 2001), and density and spectroscopic fluctuations (Burba, Anderson, & Komissarov, 2019; Webb, Pearman, & Leuning, 1980). Additional attenuation proposed by Burba et al. (2019) was applied to account for the base differences between the open-path N_2O sensor and the anemometer or the LI-7500. Finally, the one-dimensional flux density distribution was estimated based on the analytical model developed by Kljun, Calanca, Rotach, and Schmid (2004) to determine footprints of the fluxes (upwind distance that recovered 70% of the flux).

Two types of random errors were estimated, including (1) total random errors (σ_{cov}) and (2) random errors due to instrumental noise ($\sigma_{\mathrm{cov}}^{\mathrm{instr}}$) (Mauder et al., 2013). Note that σ_{cov} includes $\sigma_{\mathrm{cov}}^{\mathrm{instr}}$, and we calculated $\sigma_{\mathrm{cov}}^{\mathrm{instr}}$ to investigate sensor performance during the campaigns and how sensor performance impacts σ_{cov}.

Total random errors (σ_{cov}) were calculated as Mauder et al., (2013):

$$\sigma_{\overline{w's'}} = \sqrt{\frac{1}{n}\sum_{p=-m}^{m}\left(\overline{w'w'_p}\cdot\overline{s's'_p} + \overline{w's'_p}\cdot\overline{s'w'_p}\right)} \tag{S14}$$

where $\overline{w'w'_p}$ and $\overline{s's'_p}$ are the auto-covariances with lag p for the vertical wind and a specific tracer with lag p, $\overline{w's'_p}$ is the cross-covariance with lag p on s while $\overline{s'w'_p}$ is for lag p on w. The summation bound m equals to $n/2$ (n=18000 for 30-min EC calculation with 10-Hz measurements).

Random errors of EC calculation associated with the instrumental noise ($\sigma_{\mathrm{cov}}^{\mathrm{instr}}$) were calculated following Mauder et al. (2013). The basic assumption is that the instrumental noise is uncorrelated with the true signal then the noise term only appears at zero lag in the autocovariance:

$$C_{11}(p) = \begin{cases} \overline{x'x'_p}, & p > 0 \\ \overline{x'^2} + \overline{\varepsilon x^2}, & p = 0 \end{cases} \tag{S15}$$

where x' is the deviation from the mean; εx is the noise error, and the subscript p denotes the same quantity as without the subscript but shifted in time by p seconds. The variance of the noise error can, therefore, be estimated as:

$$\overline{\varepsilon x^2} = C_{11}(0) - C_{11}(p \to 0) \tag{S16}$$

where $C_{11}(p \to 0)$ is $C_{11}(p)$, without $C_{11}(0)$, extrapolated to zero lag. Four autocovariance terms (p = 1…4) were calculated for the extrapolation in this study following (Mauder et al., 2013). Once the variance of the noise error is calculated for vertical wind and trace gases or temperature, the $\sigma_{\overline{w's'}}^{\mathrm{instr}}$ of corresponding flux can be calculated as

$$\sigma_{\overline{w's'}}^{\text{instr}} = \sqrt{\frac{1}{n}}\sqrt{\overline{\varepsilon w^2} \cdot \overline{s'^2} + \overline{\varepsilon s^2} \cdot \overline{w'^2}} \quad \text{(S17)}$$

where n is the number of observations and $\overline{x'^2} = C_{11}(p \to 0)$.

Before calculating σ_{cov} and $\sigma_{\text{cov}}^{\text{instr}}$, time series were detrended by applying a high-pass filter with a cut-off frequency of 7.5 min to minimize impacts of the trend on auto- and cross-covariances (Mauder et al., 2013). This detrending was only done for the calculation of random errors and not for the calculation of fluxes. The two errors were calculated for covariances before applying corrections. The relative errors were calculated and multiplied with the high-frequency attenuation corrected covariances (Mauder et al., 2013). Conventionally, random errors of corrected fluxes are calculated by applying the relative errors of raw covariances to fully corrected fluxes (Foken et al., 2004; Mauder et al., 2013), which could create significant biases in random errors when corrections overwhelm the true flux. For a sensor insensitive to temperature fluctuations that have just enough sensitivity to measure background fluxes (typically with a precision better than 0.1 ppbv at 10 Hz for N_2O), the relative random error would be 100% when measuring a background level N_2O flux (e.g., 20 μg N_2O-N·m^{-2}·hr^{-1}). However, for a sensor with the same precision but requiring large corrections, the signal-to-noise ratio would be high when measuring a background flux because of the strong signals from density and spectroscopic effects (1 ppbv variations when temperature changes by 1 K for N_2O). Consequently, a low relative random error would be assigned to the measurements (10% in this case), and the instrument subject to large corrections will report a much lower random error for the corrected flux (2 μg N_2O-N·m^{-2}·hr^{-1} for 20 μg N_2O-N·m^{-2}·hr^{-1} flux) than a sensor insensitive to temperature variations. The issue is that the correction related errors are ignored. To account for the error propagations, in this study, random errors of corrected fluxes were calculated using Eq. (4) listed in the main text. The detection limit of the EC system was determined as $1.96\sigma_{F_c}$ (95% CI).

Periods with non-ideal conditions for EC method were excluded by using quality control filters following Mauder et al. (2013), which defines three quality classes: 1) Class 0: high-quality data, can be used in fundamental research; 2) Class 1: moderate quality data, no restrictions for use in long term observation programs; 3) Class 2: low data quality. Quality check flags were assigned based on the steady-state tests (SST) of all fluxes and the integral turbulence characteristics (ITC) tests of u and w for u^* and w only for scalar fluxes. Only Class 0 data were used in this study. In addition to quality check flags, two filters were applied to ensure fetch requirements, and vertical mixing conditions. First, only measurements with 70% flux occurring within the cornfield were used for the following analyses. Footprints of the flux measurements were estimated using the model developed by Kljun et al. (2004). Second, a frictional velocity (u_*) threshold of 0.1 $m \cdot s^{-1}$ was determined by checking the relationship between u_* and nighttime CO_2 and N_2O fluxes measured at the site (Nemitz et al., 2018). Fluxes below estimated flux detection limits were included in the analysis to avoid biases as suggested by Langford et al. (2015).

VI. SC flux measurements and uncertainty estimates for SC and EC comparison

The SC measurement procedure has been described by Oates et al. (2016), and a brief overview of the procedure is provided here. SC measurements were made between 10:00 and 16:00 local time. The first step was to insert bases of the cylindrical chamber about 5 cm below the soil surface, which was completed weeks before the measurements. The cylindrical chamber had a diameter of 28.5 cm and a height of about 17 cm, providing an effective headspace volume of 10 L with the lid installed. The lid had a septum for gas extraction and a 2-mm diameter venting tube for pressure equilibration. Headspace gas was extracted immediately following lid installation with a 10-ml nylon syringe and a 23-gauge needle. Three more extractions were made at 20-min intervals over a 60-min period. The extracted gases were injected into 5.9-ml Exetainer glass vials (Labco Limited, Buckinghamshire, UK). Standard gases (1 ppmv N_2O, 1 ppmv CH_4, and 400 ppmv CO_2) and ambient air were also loaded into vials to evaluate potential sample losses prior to concentration measurements by gas chromatography using an electron

capture detection (micro-ECD, Agilent 7890A GC System, California, USA) for N_2O. Visual inspection of N_2O accumulation curves identified samples with lost pressure or other measurement problems, for which fluxes were discarded. Linear regressions were performed to fit gas concentration against time. The intercepts from the regressions were compared with N_2O concentrations measured by the open-path sensor in 2016 (see Fig. S7). The SC fluxes were estimated using the slopes of the regressions.

In 2015, N_2O soil fluxes from 12 locations in the field were measured simultaneously on 5 days after planting and after application of fertilizers. Figure S10 shows the locations of the chambers. In 2016, a pair of chambers were used to measured soil N_2O flux at the same time with one chamber on the fertilization slit and another one positioned away from the slit but not on the plant. Although the spatial coverage of SC measurements decreased in 2016, the measurements were made more frequently, leading to a better temporal coverage. SC fluxes were averaged spatially to compare with N_2O EC fluxes. Because there were temporal gaps in the EC measurements due to instrument conditions as well as non-ideal atmospheric conditions for the EC method, mean values of N_2O EC fluxes observed 2 hours before and 2 hours after the corresponding SC measurement were used for the comparison. Time windows of ±1 and ±3 hours were also used to investigate impacts of temporal averaging on the SC and EC comparison.

Spatial and temporal variations of N_2O fluxes and random errors were considered for the comparison between SC and EC fluxes. For the SC fluxes, the uncertainties of the measurements were largely caused by spatial variations, which were calculated as the standard deviations of concurrent SC measurements. For the EC measurements, random errors and temporal variations were considered as

$$\sigma_{F_c}^{\tau} = \sqrt{\frac{\sum_{t=t_0-\tau}^{t=t_0+\tau}(F_c^t - \overline{F_c})^2}{N-1} + \frac{\sum_{t=t_0-\tau}^{t=t_0+\tau}\left(\sigma_{F_c}^{t=t_0}\right)^2}{N^2}} \quad \text{(S18)}$$

where $\pm\tau$ is the temporal window, N is the number of samples within the temporal window. When there was only one sample within the temporal window, only the random error of the corrected flux was considered.

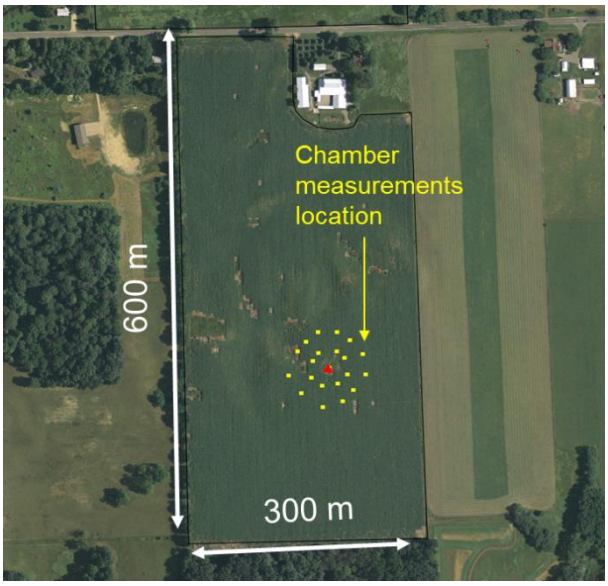


Figure S10. *Locations of static chamber measurements in 2015.*

VII. Measured EC fluxes

Figure S11 shows time series of observed N_2O concentrations by the open-path N_2O sensor and SC samples, ambient temperatures, corrected N_2O EC fluxes, and N_2O SC fluxes. In 2015, N_2O concentrations observed by the open-path N_2O sensor showed strong variations because of the drifting issue. In 2016, the drifts were much smaller and showed consistent pattern with the intercepts obtained from SC samples (see Fig. S7 for the comparison between EC and SC N_2O concentrations).

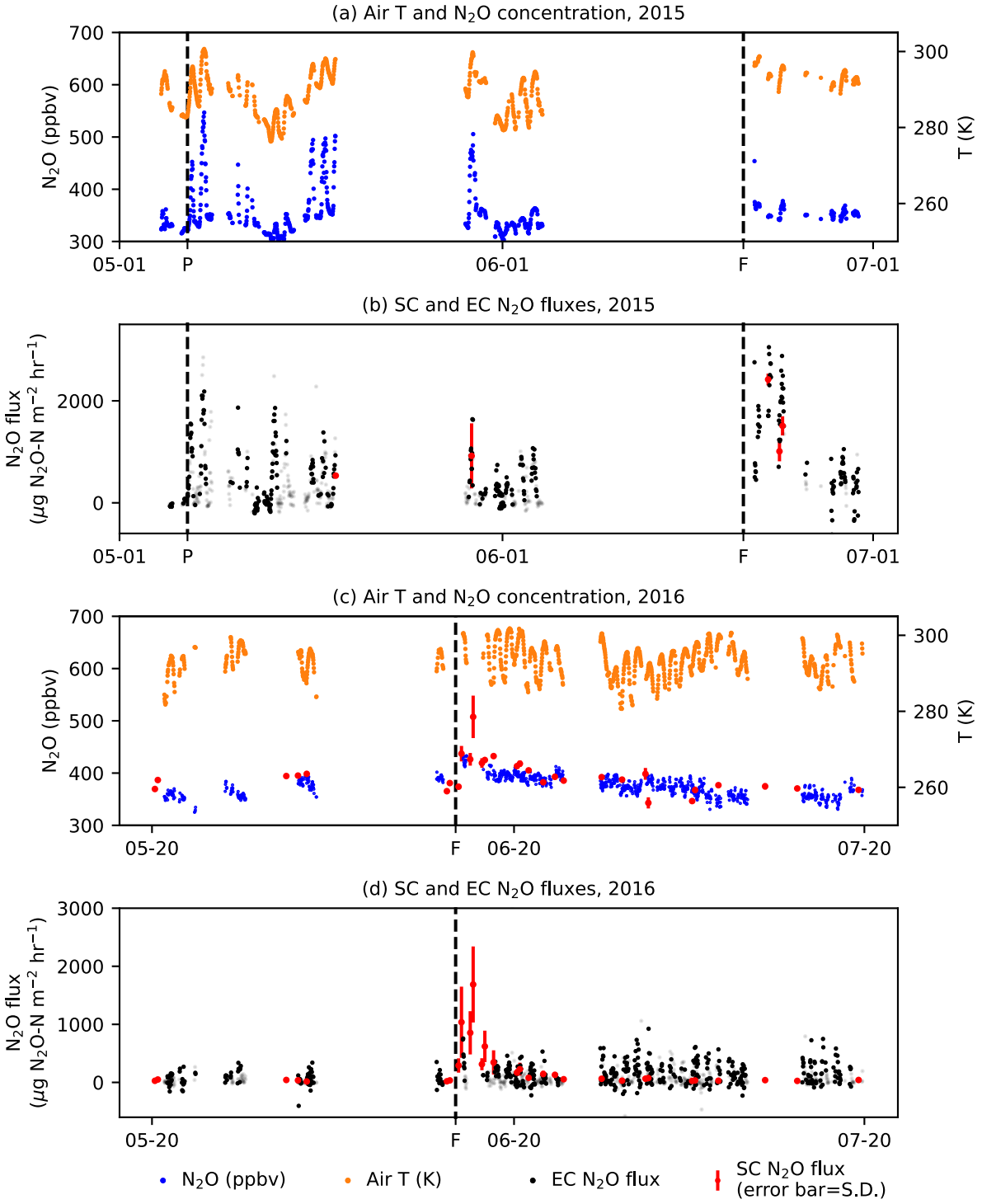


Figure S11. *Time series of observed N_2O concentrations (blue dots), temperatures (orange dots), eddy covariance (EC) N_2O fluxes (black dots), and static chamber (SC) N_2O initial concentrations and fluxes (red dots). Dashed lines indicate planting and fertilization dates.*

As discussed in Section V, 5-min rolling average was used to detrend 2015 N_2O observations before calculating the N_2O EC fluxes. To investigate the potential impacts of removing true flux signals due to the 5-min rolling average detrending, we applied the same detrend to the 2016 dataset and compared the results with the EC flux calculated using a block detrend. The results are shown in Fig. S12. We found the influence of using the 5-min rolling average detrending on observations without drifts was negligible after quality control, indicating that contribution of low-frequency signals (with a period longer than 5 min) at the site is insignificant. In 2015, however, removing 5-min rolling average leads to a larger change than in 2016, showing the impacts of the drifts.

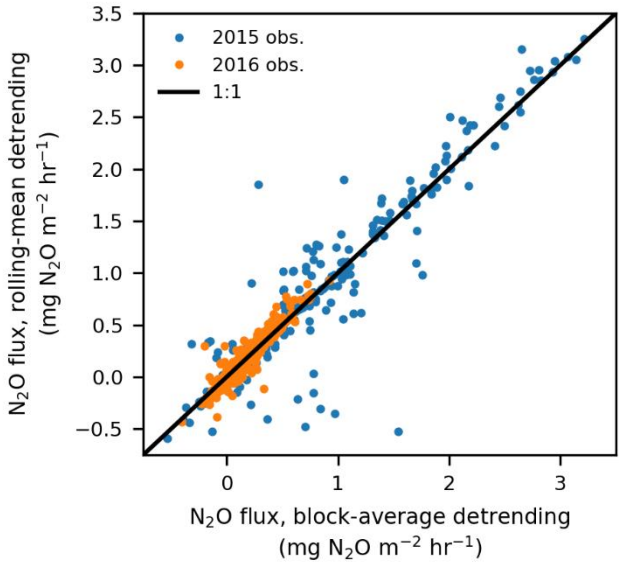


Figure S12. *Comparisons between N_2O EC fluxes in 2015 and 2015 calculated using block-average and rolling-mean detrendings.*

In 2015, the sensor's power consumption was around 50 W and had frequent shutdowns. As a result, the uptime of the sensor was around 25% of the time from May to July. In 2016, power consumption of the sensor was reduced to around 30 – 40 W, and automatic start and stop function was added to preserve the batteries. Therefore, the sensor uptime was around 34% in 2016. Table S2 and Table S3 list data coverages during daytime and nighttime. Statistics for data that were removed according to quality control and filtering described in SI Section V are also listed in Table S2 and Table S3 for comparison. Diel and daytime means of N_2O fluxes and corrections are reported in Table 2 in main text.

Table S2. Statistics of quality control and random errors of the N_2O EC flux in 2015 (as standard deviations).

Quality flag	Filter applied	Count	Fraction	Absolute instrument error (mean)	Absolute instrument error (median)	Absolute error of raw flux (mean)	Absolute error of raw flux (median)	Absolute error of corrected flux (mean)	Absolute error of corrected flux (median)	Relative instrument error (mean)	Relative instrument error (median)	Relative error of raw flux (mean)	Relative error of raw flux (median)	Relative error of corrected flux (mean)	Relative error of corrected flux (median)
Unit			%	μg N_2O-$N \cdot m^{-2} \cdot hr^{-1}$	μg N_2O-$N \cdot m^{-2} \cdot hr^{-1}$	μg N_2O-$N \cdot m^{-2} hr^{-1}$	μg N_2O-$N \cdot m^{-2} hr^{-1}$	μg N_2O-$N \cdot m^{-2} hr^{-1}$	μg N_2O-$N \cdot m^{-2} hr^{-1}$	%	%	%	%	%	%
Class 0, daytime	All	231	19	42	31	115	89	115	89	11	5	22	14	30	11
	Fetch	230	19	42	31	115	90	116	90	11	5	22	14	30	11
	& u*	225	18	43	31	117	91	118	91	11	5	22	14	31	11
Class 0, nighttime	All	152	11	24	16	45	28	45	28	19	11	27	17	60	21
	Fetch	120	8	27	17	49	29	50	29	19	12	27	16	60	22
	& u*	113	8	29	17	50	30	50	30	20	12	25	17	60	22
Class 0 & 1, daytime	All	312	25	40	29	109	84	110	85	10	4	22	14	29	12
	Fetch	306	25	40	30	110	85	111	86	10	4	22	14	29	11
	& u*	281	23	42	30	113	86	114	87	10	4	22	13	28	11
Class 0 & 1, nighttime	All	273	19	21	13	39	24	39	24	19	11	32	19	59	22
	Fetch	195	13	22	14	42	25	43	25	19	10	31	18	59	22
	& u*	157	11	25	16	45	25	45	25	19	11	26	17	52	20
Total, daytime	All	333	27	39	28	106	82	107	82	10	5	22	14	30	12
	Fetch	322	26	40	29	108	83	108	84	10	4	21	14	29	11
	& u*	285	23	42	30	112	86	113	86	10	5	22	13	28	11
Total, nighttime	All	328	23	22	12	42	24	42	24	20	11	44	21	83	23
	Fetch	224	15	20	12	43	24	43	24	19	10	47	20	86	23
	& u*	158	11	25	16	45	25	45	25	19	11	33	17	52	20

Table S3. Statistics of quality control and random errors of the N_2O EC flux in 2016 (as standard deviations).

Quality flag	Filter applied	Count	Fraction	Absolute instrument error (mean)	Absolute instrument error (median)	Absolute error of raw flux (mean)	Absolute error of raw flux (median)	Absolute error of corrected flux (mean)	Absolute error of corrected flux (median)	Relative instrument error (mean)	Relative instrument error (median)	Relative error of raw flux (mean)	Relative error of raw flux (median)	Relative error of corrected flux (mean)	Relative error of corrected flux (median)
			%	μg N_2O-$N \cdot m^{-2} hr^{-1}$	μg N_2O-$N \cdot m^{-2} hr^{-1}$	μg N_2O-$N \cdot m^{-2} hr^{-1}$	μg N_2O-$N \cdot m^{-2} hr^{-1}$	μg N_2O-$N \cdot m^{-2} hr^{-1}$	μg N_2O-$N \cdot m^{-2} hr^{-1}$	%	%	%	%	%	%
Class 0, daytime	All	433	33	34	20	42	37	43	37	26	18	49	35	295	23
	Fetch	430	33	35	20	42	37	43	37	26	18	49	34	297	23
	& u*	422	32	35	20	43	37	43	38	26	18	49	35	302	23
Class 0, nighttime	All	150	10	13	9	15	12	15	12	26	17	33	24	102	20
	Fetch	138	9	14	10	15	12	16	13	26	17	33	24	109	23
	& u*	112	7	15	11	16	13	15	13	28	19	33	24	129	23
Class 0 & 1, daytime	All	517	39	37	19	42	37	42	37	30	20	57	37	490	25
	Fetch	511	39	37	19	42	37	43	37	30	20	57	37	495	26
	& u*	483	37	38	20	43	37	43	38	30	20	57	38	519	25
Class 0 & 1, nighttime	All	284	18	13	8	14	11	14	12	28	18	38	27	100	24
	Fetch	242	16	13	8	14	11	14	12	28	18	38	27	111	25
	& u*	137	9	16	11	16	14	16	14	32	21	39	26	142	24
Total, daytime	All	538	41	37	19	42	37	42	37	31	20	58	38	468	26
	Fetch	532	40	38	19	42	37	43	37	31	20	58	38	474	27
	& u*	488	37	39	20	43	37	43	38	32	20	59	38	511	26
Total, nighttime	All	424	27	16	6	17	10	17	10	40	18	66	30	101	29
	Fetch	340	22	17	6	14	10	14	10	42	19	68	30	114	30
	& u*	140	9	30	11	16	14	16	14	65	22	98	27	136	25

VIII. Flux random errors and detection limits

Figure S13 shows three types of random errors and total random errors. Random errors caused by instrumental noise ($\sigma_{\mathrm{cov}}^{\mathrm{instr}}$) were estimated using Eq. (S17), and random errors due to stochastic nature of the turbulence were calculated as the differences between σ_{cov} and $\sigma_{\mathrm{cov}}^{\mathrm{instr}}$ (Langford et al., 2015; Mauder et al., 2013). Random errors propagated through corrections are calculated as the terms related to $\sigma_{\overline{w'T'}}$ and $\sigma_{\overline{w'\rho_v'}}$ in Eq. (4) in the main text. Contributions of these errors to random errors of the corrected N_2O flux were calculated using their squared values, assuming they are Gaussian and independent of each other.

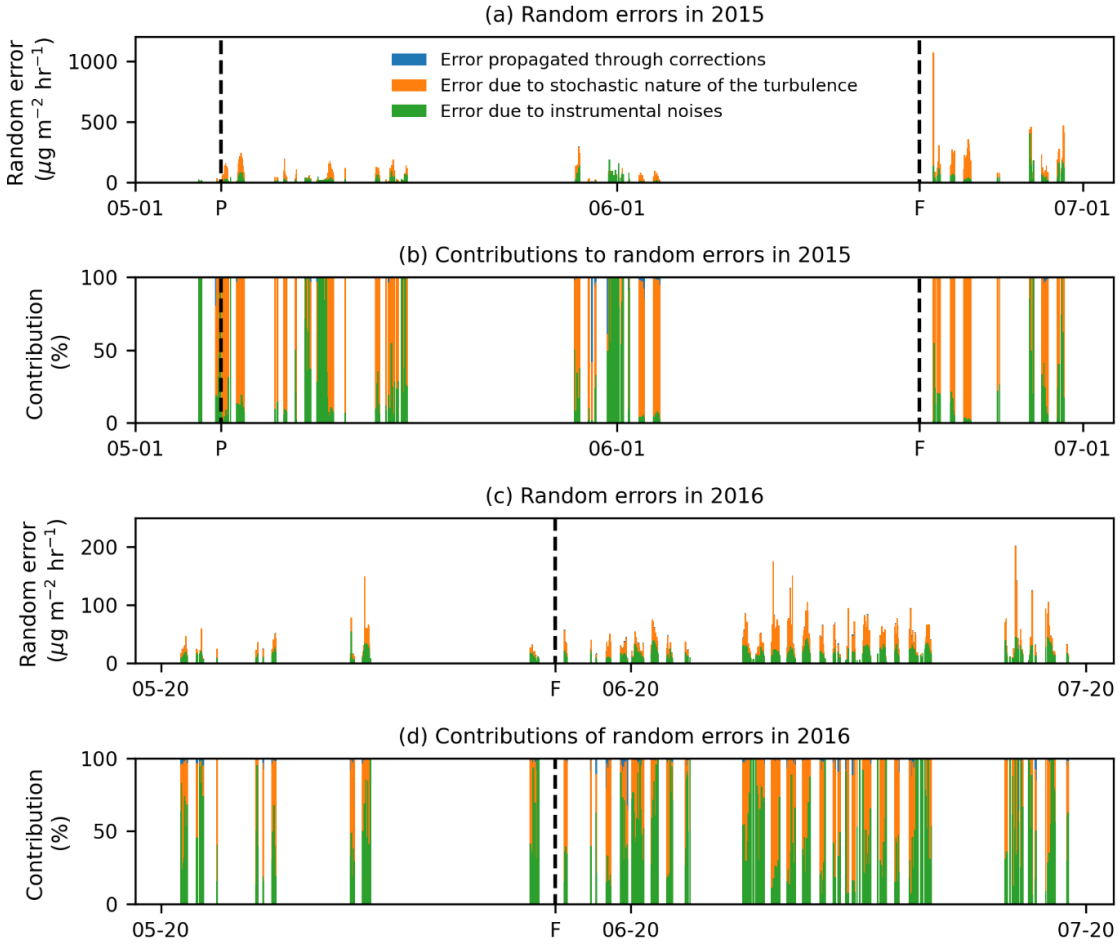


Figure S13. *Random errors (standard deviations) of the corrected N_2O fluxes and contributions of different sources. Blue areas show errors propagated through corrections. Orange areas show errors due to stochastic nature of the turbulence. And green areas show the errors caused by instrumental noises. Contributions of different types of random errors were calculated using their squared values assuming they are independent to each other.*

The median (mean) values of σ_{F_c} were 71 (95) and 32 (38) μg N_2O-N·m^{-2}·hr^{-1} for Class 0 data in 2015 and 2016, respectively. Defining $1.96\sigma_{F_c}$ as the detection limit (95% CI), the median detection limits were 139 and 63 μg N_2O-N m^{-2} hr^{-1} in 2015 and 2016, respectively. The detection limit in 2015 was impacted by large N_2O emissions from fertilizations applied during planting. The median detection limit in 2016 is 50%, 70%, and 330% larger than the detection limits reported by Kroon et al. (2010), Neftel et al. (2010), and Huang et al. (2014) for closed-path N_2O systems. Diel and daytime means of corresponding detection limits are reported in Table 2 in the main text. Daytime and nighttime random errors are also listed in Table S2 and Table S3.

The median (mean) values of $\sigma_{\mathrm{cov}}^{\mathrm{instr}}$ were 31 (42) and 20 (34) μg N_2O-N·m^{-2}·hr^{-1}, contributing (squared contributions to square sum errors) to 14% (30%) and 32% (41%) of total random errors of the corrected N_2O fluxes, in 2015 and 2016, respectively. The contribution of instrumental noises to total random errors of N_2O fluxes were much higher than those of sensible and latent heat fluxes, which were around 4 – 6%, highlighting the challenges associated with measuring N_2O precisely at high frequency. Because of low $|M_T|$, the random errors propagated through corrections had small contributions (1 – 3%) to the random errors of the corrected N_2O fluxes. This also means that improving sensor precision in the future can significantly reduce flux detection limit.

IX. Cospectra and high-frequency attenuation

Figure S14 shows the cospectra of quality controlled sensible heat, CO_2, H_2O, and N_2O fluxes for unstable and stable conditions in 2015 and 2016, respectively. Overall, the cospectra of N_2O fluxes are consistent with the cospectra of sensible heat for normalized frequencies below 1 Hz. In 2015, rolling-mean detrending was used to reduce the impacts of drift. However, as shown in the cospectra, there was no significant attenuation of low-frequency signals, consistent with the results shown in Fig. S12.

High-frequency attenuations (HFAs) were not observed for the N_2O fluxes despite having a longer averaging-path (30 cm) than the LI-7500 (12.5 cm). Both the open-path N_2O and the LI-7500 were positioned 20 – 30 cm from the anemometer. Under stable conditions ($L/(z\text{-}d)>0.05$), the contribution of the high-frequency signal even increased in the high frequency domain (>1 Hz). This might result from a low signal-to-noise ratio (SNR) for small N_2O fluxes as demonstrated by Langford et al. (2015). Because of this limitation, the theoretical method proposed by Moore (1986) using transfer functions was used to estimate high-frequency attenuations instead of using the Ogive curve method as proposed by Ammann, Brunner, Spirig, and Neftel (2006). The HFAs were estimated to be about 15% in both 2015 and 2016.

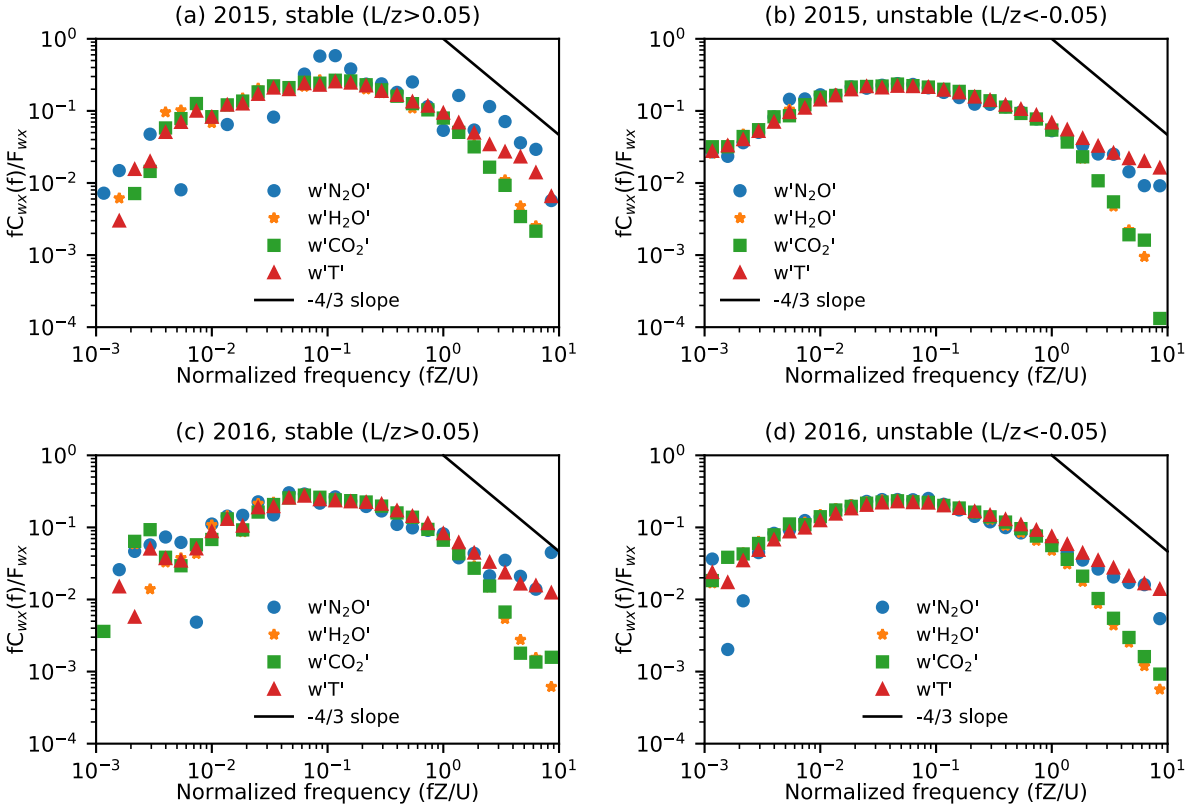


Figure S14. Ensemble average cospectra of N_2O, H_2O, CO_2, and sensible heat fluxes for stable and unstable conditions in 2015 and 2016. Only fluxes above detection limits were included.

X. Comparisons between SC and EC fluxes with time windows of ±1 hour and ±3 hours

Figure S15 shows comparisons between SC and EC fluxes with time windows of ±1 hour and ±3 hours. Using time windows of ±1 hour and ±3 hours only leads to minor changes in the regression results.

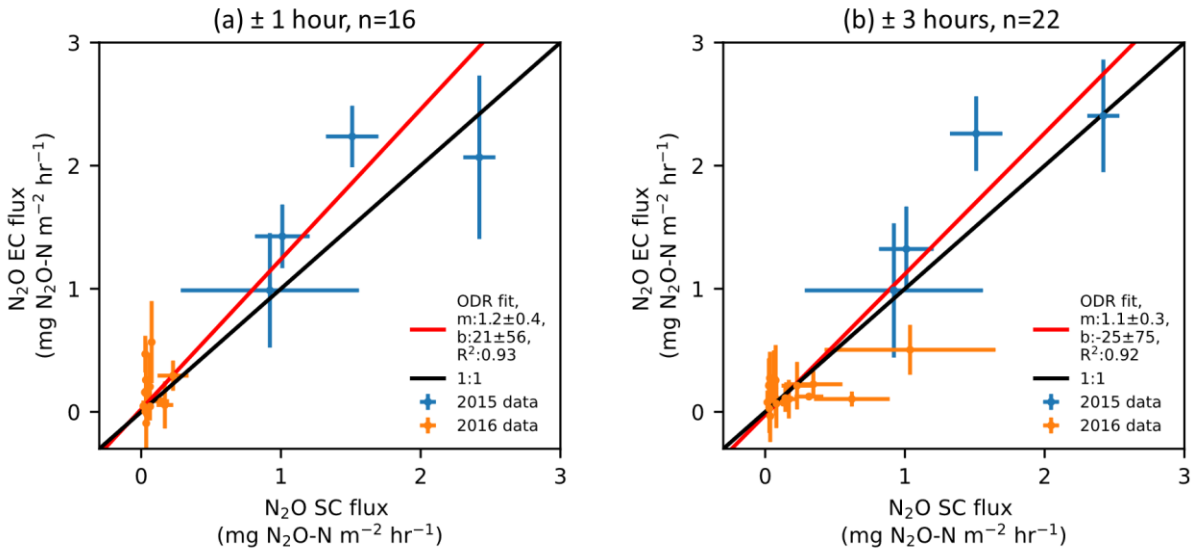


Figure S15. *Comparison between EC and SC N_2O fluxes with temporal windows of (a) ±1 and (b) ±3 hours. Vertical error bars show the standard deviation of EC observations made within the temporal windows of the SC measurement time. Horizontal error bars show the standard deviation of SC measurements made at different locations of the field. The red line shows error-weighted orthogonal distance regression (ODR) result using both 2015 and 2016 observations. The uncertainties for the ODR results are 95% CI.*

Supplementary references

Ammann, C., Brunner, A., Spirig, C., & Neftel, A. (2006). Water vapour concentration and flux measurements with PTR-MS.

Burba, G., Anderson, T., & Komissarov, A. (2019). Accounting for spectroscopic effects in laser-based open-path eddy covariance flux measurements. *Global Change Biology, 25*(6), 2189-2202.

Deng, H., Sun, J., Liu, N., Wang, H., Yu, B., & Li, J. (2017). Impact of H_2O broadening effect on atmospheric CO and N2O detection near 4.57μm. *Journal of Molecular Spectroscopy, 331*, 34-43. doi:https://doi.org/10.1016/j.jms.2016.11.001

Foken, T., Göockede, M., Mauder, M., Mahrt, L., Amiro, B., & Munger, W. (2004). Post-field data quality control. In *Handbook of Micrometeorology* (pp. 181-208): Springer.

Gamache, R. R., Hawkins, R. L., & Rothman, L. S. (1990). Total internal partition sums in the temperature range 70–3000 K: atmospheric linear molecules. *Journal of molecular spectroscopy, 142*(2), 205-219.

Gordon, I. E., Rothman, L. S., Hill, C., Kochanov, R. V., Tan, Y., Bernath, P. F., . . . Chance, K. (2017). The HITRAN2016 molecular spectroscopic database. *Journal of Quantitative Spectroscopy and Radiative Transfer, 203*, 3-69.

Huang, H., Wang, J., Hui, D., Miller, D., Bhattarai, S., Dennis, S., . . . Reddy, K. (2014). Nitrous oxide emissions from a commercial cornfield (Zea mays) measured using the eddy-covariance technique. *Atmospheric Chemistry & Physics 14*(14).

Kljun, N., Calanca, P., Rotach, M., & Schmid, H. (2004). A simple parameterisation for flux footprint predictions. *Boundary-Layer Meteorology, 112*(3), 503-523.

Kochanov, R. V., Gordon, I., Rothman, L., Wcisło, P., Hill, C., & Wilzewski, J. (2016). HITRAN Application Programming Interface (HAPI): A comprehensive approach to working with spectroscopic data. *Journal of Quantitative Spectroscopy and Radiative Transfer, 177*, 15-30.

Kroon, P., Hensen, A., Jonker, H., Ouwersloot, H., Vermeulen, A., & Bosveld, F. (2010). Uncertainties in eddy covariance flux measurements assessed from CH_4 and N_2O observations. *Agricultural and Forest Meteorology, 150*(6), 806-816.

Lacome, N., Levy, A., & Guelachvili, G. (1984). Fourier transform measurement of self-, N_2-, and O_2-broadening of N_2O lines: temperature dependence of linewidths. *Applied Optics, 23*(3), 425-435.

Langford, B., Acton, J., Ammann, C., Valach, A., & Nemitz, E. (2015). Eddy-covariance data with low signal-to-noise ratio: time-lag determination, uncertainties and limit of detection. *Atmospheric Measurement Techniques, 8*, 4197-4213.

Liu, H., Peters, G., & Foken, T. (2001). New equations for sonic temperature variance and buoyancy heat flux with an omnidirectional sonic anemometer. *Boundary-Layer Meteorology, 100*(3), 459-468.

Mauder, M., Cuntz, M., Drüe, C., Graf, A., Rebmann, C., Schmid, H. P., . . . Steinbrecher, R. (2013). A strategy for quality and uncertainty assessment of long-term eddy-covariance measurements. *Agricultural and forest meteorology, 169*, 122-135.

McDermitt, D., Burba, G., Xu, L., Anderson, T., Komissarov, A., Riensche, B., . . . Oechel, W. (2011). A new low-power, open-path instrument for measuring methane flux by eddy covariance. *Applied Physics B, 102*(2), 391-405.

Moore, C. J. (1986). Frequency response corrections for eddy correlation systems. *Boundary-Layer Meteorology, 37*(1-2), 17-35.

Moore, S. (1982). Attenuation compensation. In *Computed Emission Tomography*.

Neftel, A., Ammann, C., Fischer, C., Spirig, C., Conen, F., Emmenegger, L., . . . Wahlen, S. (2010). N_2O exchange over managed grassland: Application of a quantum cascade laser spectrometer for micrometeorological flux measurements. *Agricultural and Forest Meteorology, 150*(6), 775-785.

Nemitz, E., Mannarella, I., Ibrom, A., Aurela, M., Burba, G. G., Dengel, S., . . . Herbst, M. (2018). Standardisation of eddy-covariance flux measurements of methane and nitrous oxide. *International Agrophysics, 32*(4), 517-549.

Newville, M., Stensitzki, T., Allen, D. B., Rawlik, M., Ingargiola, A., & Nelson, A. (2016). LMFIT: Non-linear least-square minimization and curve-fitting for Python. *Astrophysics Source Code Library*.

Oates, L. G., Duncan, D. S., Gelfand, I., Millar, N., Robertson, G. P., & Jackson, R. D. (2016). Nitrous oxide emissions during establishment of eight alternative cellulosic bioenergy cropping systems in the North Central United States. *GCB Bioenergy, 8*(3), 539-549. doi:10.1111/gcbb.12268

Sun, K., Tao, L., Miller, D. J., Khan, M. A., & Zondlo, M. A. (2013). Inline multi-harmonic calibration method for open-path atmospheric ammonia measurements. *Applied Physics B, 110*(2), 213-222.

Taipale, R., Ruuskanen, T. M., & Rinne, J. (2010). Lag time determination in DEC measurements with PTR-MS. *Atmospheric Measurement Techniques, 3*(4), 853-862.

Tan, Y., Kochanov, R., Rothman, L., & Gordon, I. (2019). Introduction of water-vapor broadening parameters and their temperature-dependent exponents into the HITRAN database: Part I—CO_2, N_2O, CO, CH_4, O_2, NH_3, and H_2S. *Journal of Geophysical Research: Atmospheres, 124*(21), 11580-11594.

Tao, L., Sun, K., Khan, M. A., Miller, D. J., & Zondlo, M. A. (2012). Compact and portable open-path sensor for simultaneous measurements of atmospheric N_2O and CO using a quantum cascade laser. *Optics Express, 20*(27), 28106-28118.

Toth, R. A. (2000). N2-and air-broadened linewidths and frequency-shifts of N_2O. *Journal of Quantitative Spectroscopy and Radiative Transfer, 66*(3), 285-304.

Webb, E. K., Pearman, G. I., & Leuning, R. (1980). Correction of flux measurements for density effects due to heat and water vapour transfer. *Quarterly Journal of the Royal Meteorological Society, 106*(447), 85-100.